A MOVING INTERFACE METHOD FOR DYNAMIC KINETIC-FLUID COUPLING [*]

Pierre Degond[†], Giacomo Dimarco[‡], and Luc Mieussens[§]

April 16, 2007

Abstract

This paper is a continuation of earlier work [6] in which we presented an automatic domain decomposition method for the solution of gas dynamics problems which require a localized resolution of the kinetic scale. The basic idea is to couple the macroscopic hydrodynamics model and the microscopic kinetic model through a buffer zone in which both equations are solved. Discontinuities or sharp gradients of the solution are responsible for locally strong departures to local equilibrium which require the resolution of the kinetic model. The buffer zone is drawn around the kinetic region by introducing a cut-off function, which takes values between zero and one and which is identically zero in the fluid zone and one in the kinetic zone. In the present paper, we specifically consider the possibilty of moving the kinetic region or creating new kinetic regions, by evolving the cut-off function with respect to time. We present algorithms which perform this task by taking into account indicators which characterize the non-equilibrium state of the gas. The method is shown to be highly flexible as it relies on the time evolution of the buffer cut-off function rather than on the geometric definition of a moving interface which requires remeshing, by contrast to many previous methods. Numerical examples are presented which validate the method and demonstrate its performances.

Keywords: kinetic-fluid coupling, multiscale problems, Boltzmann equation, fluid-dynamic limit.

1   Introduction

In this work we consider the numerical simulation of fluid flows in rarefied regimes. In this situation the Navier-Stokes or the Euler equations do not provide a satisfactory description

---

of the physical system and a kinetic description through the Boltzmann equation becomes necessary. In practice, we are primarily interested in the macroscopic scales of the problems but the solution of the microscopic model is necessary to obtain the correct representation of the physical phenomena. From the computational side, the numerical solution through such microscopic models remains nowadays too expensive even with the use of supercomputers.

The most widely used numerical method for the Boltzmann equation is the Direct Simulation Monte-Carlo (DSMC) method (see [11], [13], [2] [24], [25], [9], [26]). It has many advantages in terms of computational efficiency for large dimensional problems and in terms of flexibility for enforcing physical properties such as conservation laws. On the other hand, these methods are only poorly accurate. They generate large fluctuations as compared to deterministic methods and the convergence rate is in general quite slow.

In situations close to thermodynamical equilibrium, the cost of direct Monte Carlo simulations increases. For this reason, domain decomposition techniques have been proposed in the literature (see [1], [21], [16], [17], [7], [10]). They allow a more efficient treatment of the regions close to thermodynamical equilibrium. Automatic domain decomposition methods have also been proposed, (see e.g. [15] or [28]). Indeed, in many situations, the resolution of the kinetic equations in the whole computational domain is unnecessary because the Euler or Navier-Stokes equations provide a sufficiently accurate solution, except in small zones like shock layers where departure from thermodynamical equilibrium is strong.

The present work is a contribution in this direction. We propose a numerical method for the resolution of the Boltzmann-BGK equation coupled with the compressible Euler equations through a domain decomposition technique. The validity of BGK model is sometimes questionnable. However it provides a cheaper model than the full Boltzmann equation, in particular close to the fluid regime where the DSMC method is extremely expensive. Anyhow, our approach can be applied to the full Boltzmann model as well without any change, and our choice of the BGK equation is just a matter of convenience. We could also choose the Navier-Stokes model instead of the Euler model as a fluid model.

This paper is an extension of an earlier work [6], in which the domain decomposition technique is used to couple the BGK equation and the compressible Euler equations. In this earlier work, a buffer zone is introduced. In this buffer zone, the transition from the Boltzmann model to the hydrodynamic one and vice-versa is gradual. Therefore, in the buffer zone, both models are solved and the solution of the problem is obtained as the combination of the kinetic and fluid solutions. The buffer zone is materialized by a cut-off function which defines the gradual transition from one model to the other one. Additionally, the introduction of the cut-off makes each of the models degenerate at the boundary of the buffer zone. In this way, no interface condition is needed.

In the present work, we propose a methodology to allow for the time evolution of the buffer zone between the kinetic and fluid models. In this way, we can follow in time the regions where discontinuities or sharp gradients of the solution occur, and solve the microscopic model in these regions, while, in the rest of the domain, we can use the macroscopic model. Thanks to this technique, it is possible to use as small a microscopic domain as possible, and to achieve considerable computational speedup compared with a

steady interface coupling strategy. An important point in implementing this method is to use adequate criteria which allow to reliably identify the zones for which the microscopic model is necessary. Another novelty of the present work is to propose the use of a new indicator, the equilibrium fraction, which has been introduced in the works of Dimarco and Pareschi in [9].

The main features of the method can be summarized as follows:

- The domain is divided in regions where the solution is computed through kinetic equations and in regions where the solution is computed through Euler equations and in buffer zones where both model are used.

- During the simulation the zones move according to some equilibrium criteria in order to solve the kinetic model only where it is necessary.

- The utilized criteria are combinations of:

  - Checking the value of the Knudsen number against an adequate threshold value
  - Checking the values of the gradients of the macroscopic quantities (density, momentum) against an adequate threshold value
  - Measuring the equilibrium fraction in the kinetic zone.

The article is organized as follows. In section 2, we introduce the Boltzmann-BGK equations and its properties. In section 3, we present the coupling method and in section 4 the numerical schemes. Section 5 is devoted to the illustration of the equilibrium identification criteria. Several test problems which demonstrate the capabilities of the method are presented in section 6. Some final considerations and future developments are discussed in section 7.

2   Boltzmann-BGK Equation

2.1   The model

We consider the Boltzmann-BGK equation

$$\partial_t f + v \cdot \nabla_x f = \frac{1}{\tau}(M_f - f), \tag{1}$$

with the initial condition

$$f(x, v, t = 0) = f_0(x, v), \tag{2}$$

where $f = f(x, v, t)$ is a non negative function describing the time evolution of the distribution of particles which move with velocity $v \in \mathbb{R}^3$ in the position $x \in \Omega \subset \mathbb{R}^3$ at time $t > 0$. In the BGK equation the collisions are modeled by a relaxation towards the local thermodynamical equilibrium defined by the Maxwellian distribution function M_f. The local Maxwellian function is defined by

$$M_f = M_f[\varrho, u, T](v) = \frac{\varrho}{(2\pi\theta)^{3/2}} \exp\left(\frac{-|u - v|^2}{2\theta}\right), \tag{3}$$

where ϱ and u are the density and mean velocity while $\theta = RT$ with T the temperature of the gas and R the gas constant. The macroscopic values ϱ, u and T are related to f by:

$$\varrho = \int_{\mathbb{R}^3} f dv, \qquad u = \int_{\mathbb{R}^3} v f dv, \qquad \theta = \frac{1}{3\varrho} \int_{\mathbb{R}^3} |v - u|^2 f dv. \tag{4}$$

The energy E is defined as

$$E = \frac{1}{2} \int_{\mathbb{R}^3} |v|^2 f dv = \frac{1}{2} \varrho |u|^2 + \frac{3}{2} \varrho \theta. \tag{5}$$

The parameter $\tau > 0$ is the relaxation time. In this paper, we use the common choice $\tau = (\frac{\mu}{p})$ where $\mu = \mu_{ref} \cdot (\theta/\theta_{ref})^\omega$ is the viscosity and p is the pressure. We refer to section 6 for the numerical value of μ_{ref}, θ_{ref} and ω. Finally we define the kinetic entropy of f by

$$H(f) = \int_{\mathbb{R}^3} f \log f dv. \tag{6}$$

Now, if we consider the BGK equation (1), multiply it by 1, v, $\frac{1}{2}|v^2|$ (the so-called collision invariants), and integrate wit respect to v, we obtain the following balance laws:

$$\frac{\partial \varrho}{\partial t} + \nabla_x \cdot (\varrho u) = 0,$$
$$\frac{\partial \varrho u}{\partial t} + \nabla_x \cdot (\varrho u \otimes u + P) = 0, \tag{7}$$
$$\frac{\partial}{\partial t} E + \nabla_x \cdot (Eu + Pu + q) = 0,$$

which express the conservation of mass, momentum and energy, in which $P = \int (v - u) \otimes (v - u) f dv$ is the pressure tensor while $q = \int \frac{1}{2}(v - u)|v - u|^2 dv$ is the heat flux. Furthermore the following inequality expresses the dissipation of entropy:

$$\partial_t \left(\int f \log f dv \right) + \nabla_x \cdot \left(\int v f \log f dv \right) \leq 0. \tag{8}$$

System (7) is not closed, since it involves other moments of the distribution function than just ϱ, ϱu and E.

The Maxwellian M_f can be characterized as the unique solution of the following entropy minimization problem

$$H(M_f) = \min\{H(f), \ f \geq 0 \ s.t. \int_{\mathbb{R}^3} \mathbf{m} f dv = \boldsymbol{\varrho}\} \tag{9}$$

where $\mathbf{m}$ and $\boldsymbol{\varrho}$ are the vectors of the collision invariants and of the first three moments of f respectively:

$$\mathbf{m}(v) = (1, v, \frac{1}{2}|v|^2), \ \boldsymbol{\varrho} = (\varrho, \varrho u, E) \tag{10}$$

This is the well-known local Gibbs principle, and it expresses that the local thermodynamical equilibrium state minimizes the entropy of all the possible states subject to the constraint that its moments $\boldsymbol{\varrho}$ are prescribed.

Formally as $\varepsilon \to 0$ the function f tends to Maxwellian. In this limit, it is possible to compute the moments P and q of f in terms of ϱ, ϱu and E. In this way, one can close the system of balance laws (7) and get the Euler system of compressible gas dynamics equations

$$
\begin{aligned}
&\frac{\partial \varrho}{\partial t} + \nabla_x \cdot (\varrho u) = 0, \\
&\frac{\partial \varrho u}{\partial t} + \nabla_x \cdot (\varrho u \otimes u + pI) = 0, \\
&\frac{\partial E}{\partial t} + \nabla_x \cdot ((E+p)u) = 0, \\
&p = \varrho\theta, \quad E = \frac{3}{2}\varrho\theta + \frac{1}{2}\varrho|u|^2.
\end{aligned}
\tag{11}
$$

2.2 Boundary Conditions

Eq. (1) must be supplemented with boundary conditions for $x \in \partial\Omega$ and for $v \cdot n \geq 0$ where n denotes the unit normal, pointing inside the domain. The boundary conditions are expressed as follows:

$$
|v \cdot n| f(v) = \int_{v_* \cdot n < 0} |v_* \cdot n| K(v_* \to v) f(v_*) dv_* ,
\tag{12}
$$

where v_* is the particle velocity after its interaction with the boundary. The entering flux is described as a function of the outgoing flux modified by the boundary kernel K. Such a definition of the boundary condition preserve the mass if and only if

$$
K(v_* \to v) \geq 0, \ \int_{v_* \cdot n \geq 0} K(v_* \to v) dv = 1.
\tag{13}
$$

Usually, the boundary condition is a convex combination of specular reflection and total accomodation. Specular reflection is the process by which the incoming velocity (i.e. after the interaction with the wall) is the symmetric of the outgoing velocity with respect to the tangent plane to the wall. Total accomodation instead means that the outgoing velocity loses the memory of the incoming velocity and is taken randomly according to a Maxwellian distribution at the wall temperature. Let α be the fraction of particles which suffer total accomodation and $1 - \alpha$ that of specularly reflected particles. With these assumptions, the boundary condition is written:

$$
f(v) = (1 - \alpha) Rf(v) \alpha M f(v), \ v \cdot n(x) \geq 0,
\tag{14}
$$

with

$$
Rf(v) = f(v - 2n(n \cdot v)), \quad M f(v) = \mu M_\omega(v).
\tag{15}
$$

If we denote by u_w and θ_w the wall velocity and temperature, M_w is given by

$$
M_w[u_w, \theta_w](v) = \frac{1}{(2\pi\theta_w)^{3/2}} \exp\left(\frac{-|u_w - v|^2}{2\theta_w}\right),
\tag{16}
$$

and μ is determined by mass conservation

$$\mu \int_{v \cdot n \geq 0} M_w(v)|v \cdot n|dv = \int_{v \cdot n < 0} f(v)|v \cdot n|dv. \tag{17}$$

It is easy to show that this boundary condition enters the class of boundary conditions of the type (12), with a suitably defined (and possibly distributional) kernel K. We note that for $\alpha = 0$ (pure specular reflection) the re-emitted particle have the same flow of mass, energy and tangential momentum as the incoming molecules, while as soon as $\alpha > 0$ (partial or full accommodation) the re-emitted particle partly or completely lose the memory of the incoming velocities. In particular, only mass is conserved.

3 The coupling method

3.1 Decomposition of the kinetic equation

For sake of simplicity we describe the method proposed in [6] in one space and velocity dimensions. It can be easily extended to a generic N-dimensional setting. Also different meshes for the cut-off function and for the other variables can be used.

We denote the buffer interval by $[a, b]$, and we introduce a cut-off function $h(x, t)$ such that

$$h(x, t) = \begin{cases} 1, & \text{for} \quad x \leq a \\ 0, & \text{for} \quad x \geq b \\ 0 \leq h(x, t) \leq 1, & \text{for} \quad x \in [a, b] \end{cases} \tag{18}$$

For instance, h can be chosen piecewise linear in $[a, b]$:

$$h(x, t) = \frac{x - b}{a - b} \quad \text{for} \quad x \in [a, b].$$

We define two distribution functions such that $f_R = hf$ while $f_L = (1 - h)f$. We look now for an evolution equation for f_R and for f_L. We write

$$\partial_t f_R = \partial_t (hf) = f \, \partial_t h + h \partial_t f,$$
$$\partial_t f_L = \partial_t ((1 - h)f) = -f \, \partial_t h + (1 - h)\partial_t f.$$

Thus multiplying the Boltzmann-BGK equation (1) by h and $1 - h$ respectively, (1) can be rewritten in the following form

$$\partial_t f_R = f \, \partial_t h + h(-v\partial_x f + \frac{1}{\tau}(M_f - f)),$$

$$\partial_t f_L = -f \, \partial_t h + h(-v\partial_x f + \frac{1}{\tau}(M_f - f)),$$

which finally leads to the following system for f_L and f_R:

$$\partial_t f_R + hv\partial_x f_R + hv\partial_x f_L = \frac{h}{\tau}(M_f - f) + f\partial_t h, \tag{19}$$

$$\partial_t f_L + (1 - h)v\partial_x f_L + (1 - h)v\partial_x f_R = \frac{1 - h}{\tau}(M_f - f) - f\partial_t h, \tag{20}$$

$$f = f_R + f_L \tag{21}$$

with initial data

$$f_R(x, v, 0) = h(x, 0)f(x, v, 0)\,, \quad f_L(x, v, 0) = (1 - h(x, 0))f(x, v, 0).\qquad(22)$$

It is important to note that if $f = f_L + f_R$ is the solution of (1) with initial data (2), then (f_L, f_R) is the solution of (19-20) with initial data (22) and conversely.

3.2   Kinetic-Hydrodynamic coupling

We refer to [6] for more detail about the derivation that follows. Let us assume that the domain can be subdivided in two regions: in one of the regions, the distribution function is close to a local Maxwellian while in the other, it is far from it. We choose to set $h = 0$ in the region where f is close to the Maxwellian. Therefore, $f_L = f$ is close to its associated Maxwellian $M_{f_L} = M_f$ and we can replace the Boltzmann equation by the Euler equations without making any significant error. We also suppose that in the buffer zone, f_L remains close to the equilibrium and thus, it can be replaced by M_{f_L} in the whole interval $x < b$.

Replacing f_L by M_{f_L} in (20) and taking the hydrodynamic moments (mass, momentum and energy), leads to the following modified Euler system defined in the interval $x \le b$:

$$\frac{\partial \varrho_L}{\partial t} + (1 - h)\partial_x(\varrho_L u_L) = -(1 - h)\partial_x\left(\int_{\mathbb{R}} v f_R \, dv\right) - \varrho\partial_t h,$$

$$\frac{\partial \varrho_L u_L}{\partial t} + (1 - h)\partial_x(\varrho_L u_L^2 + p_L) = -(1 - h)\partial_x\left(\int_{\mathbb{R}} v^2 f_R \, dv\right) - \varrho u\partial_t h, \qquad(23)$$

$$\frac{\partial E_L}{\partial t} + (1 - h)\partial_x((E_L + p_L)u_L) = -(1 - h)\partial_x\left(\int_{\mathbb{R}} v \frac{|v|^2}{2} f_R \, dv\right) - E\partial_t h,$$

with initial data

$$(\varrho_L, u_L, \theta_L)|_{(x,0)} = (1 - h|_{(x,0)})(\varrho, u, \theta)|_{(x,0)}.$$

Under these assumptions, we have $f = f_R + M_{f_L}$, where f_R is a solution of:

$$\partial_t f_R + hv\partial_x f_R + hv\partial_x M[\varrho_L, u_L, \theta_L] = \frac{h}{\tau}(M_f - f) + f\partial_t h, \qquad(24)$$

in the interval $x \ge a$. The coupling model consists of system (23) for the hydrodynamic moments in the region $x \le b$ and eq. (24) for the kinetic distribution function in the region $x \ge a$.

When $h = 0$, system (23) coincides with system (11) because $f_R = 0$ and $f_L = M_{f_L}$. Moreover no boundary condition is needed at the boudary $x = b$ because $h = 1$ at this point, and the factors in front of the spatial derivatives of (23) vanish (in other words, the spatial derivatives are degenerate at $x = b$ for the fluid model). A similar remark is true for f_R. Indeed, when $h = 0$, $f_R = 0$ and no boundary condition is needed for the kinetic equation at $x = a$ because $h = 0$ at this point and the factor in front of the spatial derivatives in (24) vanishes. In the buffer zone $[a, b]$, the solution of the full kinetic problem f is computed as the sum of the Maxwellian M_{f_L} and of the function f_R. To summarize, the solution of the full kinetic problem is given by f_R if $x > b$, by M_{f_L} if $x < a$ and by $M_{f_L} + f_R$ if $x \in [a, b]$.

An important feature of the method is that it is very easy to divide the domain in more than two zones. Thus we can define as many buffers and as many kinetic regions as necessary if the macroscopic model fails to give the correct solution in different parts of the domain which are far apart from each other. In this latter case, the function h is still a piecewise linear function but there are multiple buffer zones $[a_j, b_j]$. Additionally, we can create new buffer zones and new kinetic zones during the simulation. For this purpose, one can update the cut-off function h according to convenient criteria to a new value and reset $f_R = hf$ and $f_L = (1-h)f$ at the time when h is changed. The way in which new zones are created is detailed in the next section. In the last section this technique will be tested on shock tube problems.

4 Numerical approximation of the coupled model

In this section we extend the simple numerical scheme proposed in [6] for the case of a steady buffer zone to the dynamical buffer zone case considered here. We also introduce a new scheme based on a time splitting of the equations which is able to circumvent some numerical problems that are observed with a direct discretization of the equations. Finally, we introduce a different, more efficient kinetic scheme for the solution of the Euler equations. The scheme will be shown in the last section to dramatically increase the efficiency of the code.

4.1 Velocity discretization

We introduce a Cartesian grid $\mathcal{V}$ of N nodes $v_k = k\Delta v + a$, where k is a bounded index, Δv is the grid step, and a is a constant. We denote the discrete collision invariants by $\mathbf{m}_k = (1, v_k, \frac{1}{2}|v_k^2|)$. The continuous distribution function f is approximated by a discrete velocity model $(f_k(t,x))_k$, where $f_k(t,x) \approx f(x, v_k, t)$. The fluid quantities are obtained from f_k thanks to discrete summations on $\mathcal{V}$:

$$\varrho(t,x) = \sum_k \mathbf{m}_k f_k(t,x) \, \Delta v. \tag{25}$$

The discrete velocity BGK model consists of a set of N evolution equations for f_k:

$$\partial_t f_k + v_k \cdot \nabla_x f_k = \frac{1}{\tau}(\mathcal{E}_k[\varrho] - f_k), \tag{26}$$

where $\mathcal{E}_k[\varrho]$ is an approximation of M_f such that (26) satisfies the same properties of conservation (7) and entropy (8) as the continuous model (1). Namely we have

$$\mathcal{E}_k[\varrho] = \exp(\boldsymbol{\alpha}(\varrho) \cdot \mathbf{m}_k), \tag{27}$$

where $\boldsymbol{\alpha}(\varrho)$ solves the nonlinear equation

$$\sum_k \mathbf{m}_k \exp(\boldsymbol{\alpha}(\varrho) \cdot \mathbf{m}_k) \, \Delta v = \varrho. \tag{28}$$

8

These equations can be solved by a Newton algorithm. In the velocity continuous case the parameters $\boldsymbol{\alpha}$ are

$$\boldsymbol{\alpha} = \left(\log \left(\frac{\varrho}{(2\pi\theta)^{\frac{1}{2}}} - \frac{|u|^2}{2\theta} \right), \frac{u}{\theta}, -\frac{1}{\theta} \right) \tag{29}$$

This discretization (existence, uniqueness, convergence) has been mathematically studied in [18, 20].

4.2 Space and time discretization of the kinetic part

According to the previous section, the velocity discretized version of (24) is

$$\partial_t f_{k,R} + h v_k \partial_x f_{k,R} + h v_k \partial_x \mathcal{E}_k[\boldsymbol{\varrho}_L] = \frac{h}{\tau}(\mathcal{E}_k[\boldsymbol{\varrho}] - f_k) + f_k \partial_t h, \tag{30}$$

where $f_{k,R}$ is an approximation of $f_R(t, x, v_k)$, and $\mathcal{E}_k[\boldsymbol{\varrho}_L]$ is an approximation of $M[\varrho_L, u_L, \theta_L]$ defined as in (27)–(28) with $\boldsymbol{\varrho}$ replaced by $\boldsymbol{\varrho}_L$. Finally, f_k is the global distribution defined as in the continuous case by $f_k = f_{k,R} + \mathcal{E}_k[\boldsymbol{\varrho}_L]$, and the corresponding global Maxwellian $\mathcal{E}_k[\boldsymbol{\varrho}]$ is defined accordingly with $\boldsymbol{\varrho}$ being the moments of f_k.

Consider a spatial Cartesian uniform grid defined by nodes $x_i = i\Delta x$ and a time discretization $t_n = n\Delta t$. If $f_i^n = (f_{k,i}^n)_k$ is an approximation of $(f_k(t_n, x_i))$, the moments of f_i^n are $\boldsymbol{\varrho}_i^n = \sum_k \mathbf{m}_k f_i^n \Delta v$. The corresponding discrete equilibrium is $\mathcal{E}_k[\boldsymbol{\varrho}_i^n]$ is defined as in (27)–(28)

Eq. (30) constitutes a set of linear hyperbolic equations with source terms. The transport part is simply a linear convection equation and can be approximated by any standard finite volume scheme. For the discretization in time we use an explicit Euler method. The scheme finally reads

$$\begin{aligned}
f_{k,i,R}^{n+1} = f_{k,i,R}^n &- h_i^{n+1} \frac{\Delta t}{\Delta x} \left(\phi_{i+1/2}(f_{k,R}^n) - \phi_{i-1/2}(f_{k,R}^n) \right) \\
&- h_i^{n+1} \frac{\Delta t}{\Delta x} \left(\phi_{i+1/2}(\mathcal{E}_k[\boldsymbol{\varrho}_L^n]) - \phi_{i-1/2}(\mathcal{E}_k[\boldsymbol{\varrho}_L^n]) \right) \\
&+ h_i^{n+1} \frac{\Delta t}{\tau_i^n} \left(\mathcal{E}_k[\boldsymbol{\varrho}_i^n] - f_{k,i}^n \right) + f_{k,i}^n (h_i^{n+1} - h_i^n).
\end{aligned} \tag{31}$$

For every grid function $(g_{k,i})_{k,i}$, the numerical fluxes are defined by

$$\phi_{i+1/2}(g_k) = \frac{1}{2} \left(v_k g_{k,i+1} + v_k g_{k,i} - |v_k|(g_{k,i+1} - g_{k,i}) \right). \tag{32}$$

The updated value of the function h_i^{n+1} is computed, with the criteria described in section 5, at the beginning of each time step. Thus at time step $n+1$, we compute h^{n+1} and next we compute the new value of f_R. The time step is computed through an estimate of the CFL number:

$$\Delta t \left(\max_i (\frac{1}{\tau_i^n}) + \max_k \left(\frac{|v_k|}{\Delta x} \right) \right) < 1. \tag{33}$$

9

4.3 Space and time discretization for the hydrodynamic part

A simple kinetic scheme for (23) is obtained by first discretizing (20) as we did for (19) in the section above. Then like in the continuous case, we take the moments of the corresponding discrete equation, and $f_{L,k,i}^n$ is replaced by $\mathcal{E}_k[\varrho_{L,i}^n]$. This leads to

$$
\begin{aligned}
\varrho_{i,L}^{n+1} = \varrho_{i,L}^n &- (1 - h_i^{n+1})\frac{\Delta t}{\Delta x}\sum_k \mathbf{m}_k \left(\phi_{i+1/2}(\mathcal{E}_k[\varrho_L^n]) - \phi_{i-1/2}(\mathcal{E}_k[\varrho_L^n])\right)\Delta v \\
&- (1 - h_i^{n+1})\frac{\Delta t}{\Delta x}\sum_k \mathbf{m}_k \left(\phi_{i+1/2}(f_{k,R}^n) - \phi_{i-1/2}(f_{k,R}^n)\right)\Delta v \quad\quad (34) \\
&- (h_i^{n+1} - h_i^n)\varrho_i^n.
\end{aligned}
$$

Again we first compute h^{n+1} at the beginning of the time step and afterwards, we advance ϱ_L in time. The severe time restrictions which occur with the kinetic scheme due to the relaxation parameter ε, do not occur with the hydrodynamic model. Thus, it would be possible to use different time steps for the fluid and kinetic parts of the model. We leave the implementation of this improvement to future work.

4.4 An alternative scheme: time splitting

We propose here an alternative to the previous scheme which consists of a time splitting scheme. With this scheme, the creation of new kinetic zones is simpler. It is based on a time splitting between the time evolution of h on the one hand and the transport and relaxation operators on the other hand. This splitting scheme reads:

First step: evolution of h:

$$
f_{k,i,R}^{n+\frac{1}{2}} = f_{k,i,R}^n + f_{k,i}^n(h_i^{n+1} - h_i^n), \quad\quad (35)
$$

$$
\varrho_{i,L}^{n+\frac{1}{2}} = \varrho_{i,L}^n - (h_i^{n+1} - h_i^n)\varrho_i^n, \qu\quad (36)
$$

Second step: evolution of the kinetic and fluid eqs.

$$
\begin{aligned}
f_{k,i,R}^{n+1} = f_{k,i,R}^{n+\frac{1}{2}} &- h_i^{n+1}\frac{\Delta t}{\Delta x}\left(\phi_{i+1/2}(f_{k,R}^{n+\frac{1}{2}}) - \phi_{i-1/2}(f_{k,R}^{n+\frac{1}{2}})\right) \\
&- h_i^{n+1}\frac{\Delta t}{\Delta x}\left(\phi_{i+1/2}(\mathcal{E}_k[\varrho_L^{n+\frac{1}{2}}]) - \phi_{i-1/2}(\mathcal{E}_k[\varrho_L^{n+\frac{1}{2}}])\right) \qu\quad (37) \\
&+ h_i^{n+1}\frac{\Delta t}{\tau_i^{n+\frac{1}{2}}}\left(\mathcal{E}_k[\varrho_i^{n+\frac{1}{2}}] - f_{k,i}^{n+\frac{1}{2}}\right),
\end{aligned}
$$

$$
\begin{aligned}
\varrho_{i,L}^{n+1} = \varrho_{i,L}^{n+\frac{1}{2}} &- (1 - h_i^{n+1})\frac{\Delta t}{\Delta x}\sum_k \mathbf{m}_k\left(\phi_{i+1/2}(\mathcal{E}_k[\varrho_L^{n+\frac{1}{2}}]) - \phi_{i-1/2}(\mathcal{E}_k[\varrho_L^{n+\frac{1}{2}}])\right)\Delta v \\
&- (1 - h_i^{n+1})\frac{\Delta t}{\Delta x}\sum_k \mathbf{m}_k\left(\phi_{i+1/2}(f_{k,R}^{n+\frac{1}{2}}) - \phi_{i-1/2}(f_{k,R}^{n+\frac{1}{2}})\right)\Delta v. \qu\quad (38)
\end{aligned}
$$

The first step of this scheme can be further simplified by using the following remark: since f^n and f_R^n are supposed to approximate $f(t_n)$ and $f_R(t_n)$, then we should have

$$f_R^n \approx f_R(t_n) = h(t_n)f(t_n) \approx h^n f^n. \tag{39}$$

Consequently, if we assume that f_R^n is **exactly** $h^n f^n$, then (35) reads

$$f_{k,i,R}^{n+\frac{1}{2}} = h_i^{n+1} f_{k,i}^n, \tag{40}$$

and in the same way we can obtain $\varrho_{i,L}^{n+\frac{1}{2}} = (1 - h_i^{n+1})\varrho_i^n$.

Thus relation (37) now reads

$$
\begin{aligned}
f_{k,i,R}^{n+1} = h_i^{n+1} \Bigg\{ & f_{k,i}^n - \frac{\Delta t}{\Delta x}\left(\phi_{i+1/2}(f_{k,R}^{n+\frac{1}{2}}) - \phi_{i-1/2}(f_{k,R}^{n+\frac{1}{2}})\right) \\
& - \frac{\Delta t}{\Delta x}\left(\phi_{i+1/2}(\mathcal{E}_k[\varrho_L^{n+\frac{1}{2}}]) - \phi_{i-1/2}(\mathcal{E}_k[\varrho_L^{n+\frac{1}{2}}])\right) \\
& + \frac{\Delta t}{\tau_i^{n+\frac{1}{2}}}\left(\mathcal{E}_k[\varrho_i^{n+\frac{1}{2}}] - f_{k,i}^{n+\frac{1}{2}}\right)\Bigg\}.
\end{aligned}
\tag{41}
$$

We recall that $f_{i,k}^{n+\frac{1}{2}} = f_{i,k,R}^{n+\frac{1}{2}} + \mathcal{E}_k[\varrho_{i,L}^{n+\frac{1}{2}}]$. But, we have

$$\mathcal{E}_k[\varrho_{i,L}^{n+\frac{1}{2}}] = \mathcal{E}_k[(1 - h_i^{n+1})\varrho_i^n] = (1 - h_i^{n+1})\mathcal{E}_k[\varrho_i^n],$$

because the equilibria are degree 1 homogeneous functions of ϱ. Then, with (40), we have:

$$f_{i,k}^{n+\frac{1}{2}} = h_i^{n+1} f_{i,k}^n + (1 - h_i^{n+1})\mathcal{E}_k[\varrho_i^n]. \tag{42}$$

However, according to the derivation of the coupling model the kinetic distribution function in the buffer zone must be close to the equilibrium. Assume again an exact equality, we have $f_{i,k}^n = \mathcal{E}_k[\varrho_i^n]$. Inserting this relation into (42), we deduce that

$$f_{i,k}^{n+\frac{1}{2}} = f_{i,k}^n. \tag{43}$$

Note that relation (43) is very natural, since it means that f is not changed by the evolution of the buffer zone. With this identity and the linearity of the fluxes with respect to the distribution function, we use (41) to rewrite $f_{k,i,R}^{n+1}$ as

$$
\begin{aligned}
f_{k,i,R}^{n+1} &= h_i^{n+1}\left(f_{k,i}^n - \frac{\Delta t}{\Delta x}\left(\phi_{i+1/2}(f_k^n) - \phi_{i-1/2}(f_k^n)\right) + \frac{\Delta t}{\tau_i^n}\left(\mathcal{E}_k[\varrho_i^n] - f_{k,i}^n\right)\right), \\
&:= h_i^{n+1}\tilde{f}_{k,i}^{n+1},
\end{aligned}
$$

where $\tilde{f}_{k,i}^{n+1}$ appears to be like an approximation of $f(t_{n+1})$ by an explicit time discretization. This means that our assumption (39) is also valid at time t_{n+1}. We can of course obtain similar relations for $\varrho_{i,L}^{n+1}$.

11

In summary, the time splitting scheme is written as follows:

First step (modified and simplified):

$$f_{k,i,R}^{n+\frac{1}{2}} = h_i^{n+1} f_{k,i}^n, \tag{44}$$

$$\boldsymbol{\varrho}_{i,L}^{n+\frac{1}{2}} = (1 - h_i^{n+1})\boldsymbol{\varrho}_i^n, \tag{45}$$

Second step (unchanged):

$$f_{k,i,R}^{n+1} = f_{k,i,R}^{n+\frac{1}{2}} - h_i^{n+1}\frac{\Delta t}{\Delta x}\left(\phi_{i+1/2}(f_{k,R}^{n+\frac{1}{2}}) - \phi_{i-1/2}(f_{k,R}^{n+\frac{1}{2}})\right)$$
$$- h_i^{n+1}\frac{\Delta t}{\Delta x}\left(\phi_{i+1/2}(\mathcal{E}_k[\boldsymbol{\varrho}_L^{n+\frac{1}{2}}]) - \phi_{i-1/2}(\mathcal{E}_k[\boldsymbol{\varrho_L}^{n+\frac{1}{2}}])\right) \tag{46}$$
$$+ h_i^{n+1}\frac{\Delta t}{\tau_i^{n+\frac{1}{2}}}\left(\mathcal{E}_k[\boldsymbol{\varrho}_i^{n+\frac{1}{2}}] - f_{k,i}^{n+\frac{1}{2}}\right),$$

$$\boldsymbol{\varrho}_{i,L}^{n+1} = \boldsymbol{\varrho}_{i,L}^{n+\frac{1}{2}} - (1 - h_i^{n+1})\frac{\Delta t}{\Delta x}\sum_k \mathbf{m}_k\left(\phi_{i+1/2}(\mathcal{E}_k[\boldsymbol{\varrho}_L^{n+\frac{1}{2}}]) - \phi_{i-1/2}(\mathcal{E}_k[\boldsymbol{\varrho}_L^{n+\frac{1}{2}}])\right)\Delta v$$
$$- (1 - h_i^{n+1})\frac{\Delta t}{\Delta x}\sum_k \mathbf{m}_k\left(\phi_{i+1/2}(f_{k,R}^{n+\frac{1}{2}}) - \phi_{i-1/2}(f_{k,R}^{n+\frac{1}{2}})\right)\Delta v. \tag{47}$$

In this way, at any location in space, according to certain criteria which are detailed below, the scheme can shift from a fluid model to a kinetic one and vice-versa.

4.5   An alternative scheme for the fluid equations

Our final goal is a more efficient method for computing rarefied gas dynamics problems than a full microscopic scheme, while maintaining the same accuracy. To this aim a fast numerical scheme for the fluid part of the coupling method, based on the kinetic scheme of Perthame [27] has been implemented. In the last section, we will observed that considerable speedup is obtained using this method compared with the scheme (34).

In this scheme, the true Maxwellian is replaced by the square-shaped function $M_P[\boldsymbol{\varrho}] = a\chi(v)_{-b \le v - u \le b}$, where $\chi(v)$ is a non negative function such that $\chi(v) = 1$ if $u \in [-b, b]$ and 0 elsewhere. The coefficients a and b are computed so that the moment vector of $M_P[\boldsymbol{\varrho}]$ is exactly $\boldsymbol{\varrho}$. Then, the Euler fluxes are approximated by using a kinetic flux vector splitting based on the exact integration of this approximate Maxwellian. This scheme applied to the fluid part of the coupling model then reads:

$$\frac{\boldsymbol{\varrho}_{i,L}^{n+1} - \boldsymbol{\varrho}_{i,L}^n}{\Delta t} = -(1 - h_i^{n+1})\frac{(\mathcal{F}_{i+1/2}(\boldsymbol{\varrho}_L^n) - \mathcal{F}_{i-1/2}(\boldsymbol{\varrho}_L^n))}{\Delta x}$$
$$- \frac{(1 - h_i^{n+1})}{\Delta x}\sum_k \mathbf{m}_k\left(\phi_{i+1/2}(f_{k,R}^n) - \phi_{i-1/2}(f_{k,R}^n)\right)\Delta v$$
$$+ \frac{(h_i^{n+1} - h_i^n)}{\Delta t}\boldsymbol{\varrho}_i^n, \tag{48}$$

12

where $\mathcal{F}_{i+1/2}(\boldsymbol{\varrho}_L) = \int_{v<0} v\boldsymbol{m}M_P[\boldsymbol{\varrho}_{i+1}]\,dv + \int_{v>0} v\boldsymbol{m}M_P[\boldsymbol{\varrho}_i]\,dv$.

However, for a fair analysis of the behavior of the coupling method, we used the scheme (34) in almost all the tests cases. Indeed, this scheme is constructed from the discrete moments of the scheme for the kinetic part (we could say that the schemes for both parts are 'compatible'). In this way, we avoid sources of discrepancies due to a change of the nature of the scheme for the hydrodynamic parts and our observations can really focus on the behaviour of the coupling model.

We have also observed that, although small, some oscillations appear inside the buffer zone when the Perthame scheme is used. To circumvent this problem, we use the Perthame scheme in the pure fluid region (i.e. $h = 0$) and we use the scheme (34) inside the buffer zone. The transition between the fluid and kinetic models seems to be smoother if the scheme for the fluid part in the buffer zone is compatible (in the above sense) with the scheme for the kinetic part. Outside the buffer zone, it is possible to shift to any other fluid scheme without noticeable errors.

A different approach to solve this compatibility problem would be to use the alternative coupling method proposed in [8] using a different decomposition of the distribution function f. This investigation is in progress.

5 Moving Buffer and Kinetic zones

We have already mentionned the possibility of dividing the computational domain in different regions with the introduction of several buffer and kinetic zones. Now we need an algorithm for finding the correct locations of the zones and of their motions. To this aim, we must decide where we need the microscopic model. Indeed, shock waves, contact discontinuities or rarefaction waves that are responsible of local discontinuities or sharp gradients do actually move in time. Thus, it is crucial to move the kinetic and buffer regions simultaneously with these waves in order to represent the solution with the appropriate model. Moreover we can achieve considerable computational speedup if we can use narrower kinetic zones (even of width of a few mesh points if the situation permits).

We have experimented different criteria in our simulations. Some of them can be deduced from both the macroscopic and microscopic models while other ones only depend on the microscopic model. Of course the second kind of criteria contain more information but can only be accessed to in the kinetic region.

5.1 Microscopic Criteria

The most obvious indicator of the degree of rarefaction of a gas (but not of its closedness to the local equilibrium), is the Knudsen number ε which is defined as the ratio of the mean free path of the particles λ to a reference length L:
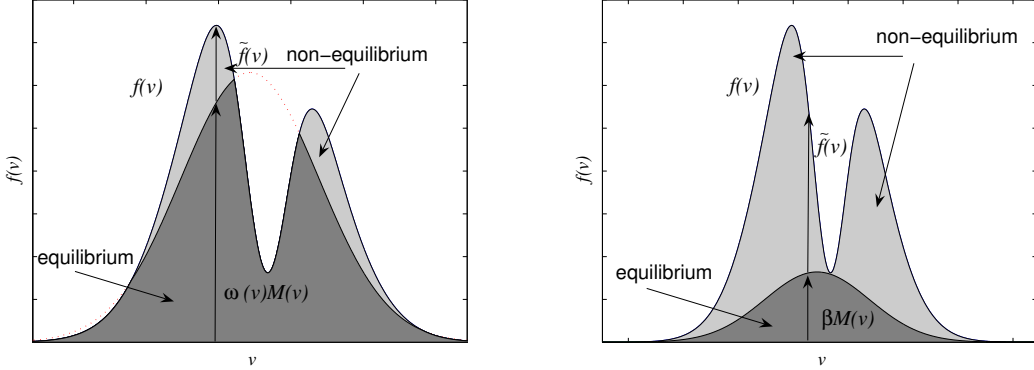
$$\varepsilon = \lambda/L,$$

Figure 1: Distribution function as a combination of equilibrium and non-equilibrium parts: representation (49) (left) and representation (51) (right).

where the mean free path is defined by

$$\lambda = \frac{kT}{\sqrt{2}\pi p\sigma_c^2},$$

with k the Boltzmann constant equal to $1.380062 \times 10^{-23} JK^{-1}$, p the pressure and σ_c the collision diameter of molecules. The Knudsen number is determined through macroscopic quantities and can be computed in the whole domain. However, it is well known that when the flow is undisturbed even in a very rarefaction regime, the hydrodynamic approximation is valid. Thus, we need a criterion to locate the discontinuities or sharp gradients inside the domain.

In kinetic regions we can utilize a new indicator, which we will call the equilibrium fraction, and which will tell us if the thermodynamical equilibrium hypothesis is correct or not. The starting point is the following definition [9]:

Definition 1 *Given a distribution function $f(v)$, and a distribution function $M(v)$, called Maxwellian, we define $\omega(v) \in [0,1]$ and $\tilde{f} \geq 0$ in the following way*

$$\omega(v) = \begin{cases} \dfrac{f(v)}{M(v)}, & f(v) \leq M(v) \neq 0 \\ 1, & f(v) \geq M(v) \end{cases}$$

and

$$\tilde{f}(v) = f(v) - \omega(v)M(v).$$

Thus $f(v)$ can be represented as (figure 1)

$$f(v) = \tilde{f}(v) + \omega(v)M(v). \tag{49}$$

14

If we take now

$$\beta = \min_v \{\omega(v)\}, \tag{50}$$

and

$$\tilde{f}(v) = f(v) - \beta M(v),$$

where $\beta M(v)$ can be seen as the largest Maxwellian smaller than $f(v)$. Thus the distribution function $f(v)$ can be written in the form [24, 25] (figure 1).

$$f(v) = \tilde{f}(v) + \beta M(v). \tag{51}$$

After each time step, once the distribution function has been updated, we proceed to the computation of β, analyze how it has evolved in the kinetic region during this time step and decide accordingly how to move the various zones. For instance in the vicinity of a shock wave, we expect β to be minimal. Thus a possible strategy is to set the kinetic region around this minimum. This strategy will be explored in the numerical tests presented in the last section.

In some cases, the parameter β may provide misleading information. One possible reason for this inaccurate indication comes from the very small values of the distribution function near the artificial boundaries of the velocity domain of the discrete Boltzmann-BGK equation. Thus the computation of the equilibrium fraction near these boundaries is very inaccurate and can lead to values of β much less than 1 which are meaningless.

Another type of inaccuracy occurs when f is very close to the local Maxwellian except in a tiny region of velocity space (see e.g. the situation depicted in figure 1 (left)). This very local departure can induce a small value of β while only a negligible fraction of the particles (in other words, a negligible fraction of the local total mass) are concerned by this departure to equilibrium. In this situation, we can still consider that the distribution function is close to equilibrium and that β provides a misleading information.

One way to circumvent the problem is to take into account the relative weight of the distribution function $f_{i,k}$ with respect to $\sum_k f_{i,k}$. Another strategy is also to measure the global mass of the equilibrium part, and which is given by

$$\varrho_E = \int_{\mathbb{R}^3} \omega(v) M(v) dv,$$

which for the discrete velocity case becomes

$$\varrho_E = \sum_{k \in \mathcal{K}} \omega_k \mathcal{E}_k,$$

and to define a new equilibrium fraction indicator as

$$\beta_M = \frac{\varrho_E}{\varrho}.$$

The parameter β_M gives us the ratio of mass of the equilibrium part to the total mass. It may happen that $\beta \ll 1$ while $\beta_M \approx 1$.

We finally observe that the parameter τ can also give us some useful information. If we split the pure BGK equation in a transport step and in a relaxation step, the latter reads

$$f^{n+\frac{1}{2}} = e^{-\frac{\Delta t}{\tau}} f + (1 - e^{-\frac{\Delta t}{\tau}}) M_f. \tag{52}$$

Thus, if τ is sufficient small compared to the other parameters, we can suppose that the distribution function relaxes to a local Maxwellian, and the fluid model can be used. On the other hand, the convection term is going to distort the distribution from equilibrium. The strength of the convection term can be estimated by the following quantity:

$$\tau^{'} = v \cdot \frac{\nabla_x f}{f}.$$

However, while τ is a quantity that can be computed from macroscopic quantities, $\tau^{'}$ is not. In order to estimate the magnitude of $\tau^{'}$ using only fluid quantities, we can measure the rates of changes of macroscopic quantities linked to f such as density, momentum and energy. Thus we can compare τ with the following quantities:

$$\frac{\nabla_x \mathcal{F}(\varrho)}{\varrho}.$$

The investigation of the validity of these indicators will be the subject of future work.

5.2   Macroscopic Criteria

Of course, we cannot use the equilibrium function indicator in the whole domain, because we can only access it in the kinetic region. Thus, we have to find other parameters that can indicate a deviation from the thermodynamical equilibrium. The idea is to make use of smoothness indicators which measure the roughness of the data. We look at the ratio of consecutive gradients for the density

$$\psi(i) = \frac{\varrho(i) - \varrho(i-1)}{\varrho(i+1) - \varrho(i)},$$

and for the velocity

$$\phi(i) = \frac{u(i) - u(i-1)}{u(i+1) - u(i)}.$$

If $\psi(i)$ and $\phi(i)$ are close to 1, then the data are smooth. while if $\psi(i)$ or $\phi(i)$ are far from unity, large variations of these quantities are present. We propose the value of such indicators in order to locate large gradient zones.

If $\psi(i) < 0$ or $\phi(i) < 0$, then slopes at neighboring points have different signs which indicates the existence of maxima or minima. On the other hand, if the gradient varies by a factor 2 between two neighboring points, we suppose that the data become unsmooth. Thus the threshold values which we have chosen for standard conditions are

$$\psi(i) < 0 \;\; \text{or} \;\; \psi(i) > 2, \tag{53}$$

and

$$\phi(i) < 0 \quad \text{or} \quad \phi(i) > 2, \tag{54}$$

meaning that if either (53) or (54) is satisfied, we must shift (or stay) in the kinetic regime.

In rarefied regimes, a shock waves is not a discontinuity any longer, but rather a region of large gradients. As a consequence, their localization becomes more difficult. The same considerations hold for rarefaction waves and contact discontinuities for which the gradients become smoother as the rarefaction increase. What happens in practice is that the value of the smoothness indicators decrease in magnitude when the Knudsen number increases. Thus we propose to link the value of the smoothness indicators to ε in such a way that, also in the rarefied regime we cab identify a departure from equilibrium. To this aim we propose that if $\varepsilon > 10^{-4}$, the criterion for shifting to the kinetic model becomes

$$\psi(i) < 0.7 \quad \text{or} \quad \psi(i) > 1.2, \tag{55}$$

and

$$\phi(i) < 0.7 \quad \text{or} \quad \phi(i) > 1.2, \tag{56}$$

Of course, it could be necessary to reduce even more the interval of the fluid regime if the gas is extremely rarefied. The indicator threshold could also be made dependent upon the mesh size and the order of the numerical scheme.

Others indicators that could be used instead of the above defined smoothness indicators are the gradient-length Knudsen numbers

$$\varepsilon_{GL\varrho} = \lambda \frac{|\nabla \varrho|}{\varrho}, \qquad \varepsilon_{GLu} = \lambda \frac{|\nabla u|}{u}.$$

Threshold values for these parameters indicating the transition from continuum to to kinetic regime which have been proposed in [17] and [15] are $\varepsilon_{GL} < 0.05$. It is argued that in this way the error between a macroscopic and a microscopic model is less than 5% [29].

Remark 1 *In principle, it is possible to use any type of numerical scheme for the solution of the coupling model for both the fluid and kinetic regions. Thus if, for instance, we use high resolution methods such as WENO schemes, we could utilize the smoother indicator defined by measuring the sum of the L^2 norms of all the derivatives of the interpolation polynomial $q_k(x)$ over one cell I_j. The relation reads*

$$IS_k = \sum_{l=1}^{r-1} \int_{x_{j-1/2}}^{x_{j+1/2}} \Delta x^{2l-1}(q_k^{(l)})^2 dx \tag{57}$$

The value of the weights w_k of the WENO method computed from the indicators IS_k can be used to identify a discontinuity.

5.3 Adaptive Kinetic/Fluid Algorithm

We have just listed some macroscopic and microscopic criteria allowing to locate the zones of strong departure to local thermodynamical equilibrium. Using the above criteria the algorithm detailed below permits to move the kinetic regions and to create new kinetic regions during the course of the simulation:

Algorithm for moving Kinetic-Fluid transition region: Assume $f^n, f_R^n, \varrho_L^n, h^n$ and h^{n+1} are known.

1. Identify the mesh points at which (53) or (54) are satisfied;

2. Check the values of the Knudsen number in the zones around the mesh points found at step 1;

3. if the Knudsen number is greater then 10^{-4}, change the threshold values to (55) and (56) and go back to 1;

4. Put a kinetic region around the mesh points at which the smoothness indicators exceed the corrected threshold value (this gives an updated h^{n+1});

5. Advance the coupled system in time by using scheme (31)–(34). If a new zone has been created, it is simpler to use the splitting scheme (44)–(47). This gives $f_R^{n+1}, \varrho_L^{n+1}$ and f^{n+1}.

6. Measure β and β_M in the kinetic zone;

7. Compute h^{n+2} by using the values of β or β_M. In our tests, we set $h_i^{n+2} = 1$ if β_i or $\beta_{M,i}$ is lower than 0.95 and 0 elsewhere. Fixed size buffer zones are created to smoothly pass from 1 to 0.

Remark 2 *The value of the Knudsen number strongly depends on the choice of the reference length. In our tests, we choose the domain size as reference length. However, this choice of reference length depends on the problem. A more universal Knudsen number can be defined choosing the gradient length defined before as reference length.*

6 Numerical tests

6.1 General setting

In this section, we present two numerical tests to illustrate the main features of the method. First the performance of the scheme is tested on the unsteady shock test problem for which the very simple structure of the solution makes the analysis easier. The second test problem is the classical Sod shock tube problem, in which the presence of contact discontinuities and rarefaction waves add new difficulties compared to the first problem. Both tests are considered in one space dimension. On each figure, we display the result obtained with the coupling model and with the hydrodynamic model. We do not show the solution of

the full kinetic equation because it is very close to that of the coupling system for both tests.

In order to obtain the correct equation of state, we use a one-dimensional velocity space model which is able to account for three-dimensional velocity effects. The model reads

$$\partial_t \begin{pmatrix} F \\ G \end{pmatrix} + v\partial_x \begin{pmatrix} F \\ G \end{pmatrix} = \nu \begin{pmatrix} M_F - F \\ TM_F - G \end{pmatrix}.$$

It is obtained from the full three-dimensional Boltzmann-BGK system by means of a reduction technique [14]. In this model, the fluid energy is given by

$$E = \sum_{k \in \mathcal{K}} \frac{1}{2} v_k^2 F_k + G_k.$$

In this way, we can recover the correct hydrodynamic limit given by the standard Euler system even with a lower dimensional velocity space.

The collision frequency is given by $\nu = \tau^{-1} = (\frac{\mu}{p})^{-1}$ where $\mu = \mu_{ref} \cdot (\theta/\theta_{ref})^\omega$ with $\mu_{ref} = 2.117 \times 10^{-5} \ Pa/s$ and $\omega = 0.81$. For our simulation we choose an Argon gas with molecular mass equal to $6.63 \times 10^{-27} \ kg$. This yields a value of the gas constant equal to $R \simeq 208$.

The computational speedup compared with a full kinetic simulation is not very large and mainly corresponds to the possibility of choosing larger timee steps for the hydrodynamic part. This is due to the fact that the hydrodynamic scheme that we use is deduced from the kinetic solver by taking discrete velocity moments. However, the coupling model is not altered if we shift to a more efficient scheme for the hydrodynamic part. In this case, considerable speedup can be achieved. In order to demonstrate this, we have repeated some of the tests with the scheme described in section 4.5. With this scheme, it is possible to achieve a dramatic speedup.

However, we have made most tests using the unefficient scheme described in section 4.3 because this scheme is directly deduced from the scheme for the kinetic part by taking discrete velocity moments. In this sense, the schemes for the kinetic and hydrodynamical parts are 'compatible'. Choosing compatible schemes for the two parts allows to focus our observations to the effect of the coupling model, thus reducing the discrepancies which would originate from the choice of the numerical scheme for the hydrodynamic part.

The thickness of the buffer zones is fixed and taken in each test problem equal to $1.5 \ m$, while the thickness of the kinetic and fluid regions vary according to the previously described criteria and can shrink to zero.

6.2 Unsteady Shock Tests

We consider an unsteady shock that propagates from left to right. The shock is produced by a specular wall at the left boundary $x = -20$. This is performed numerically by introducing an incoming Maxwellian distribution in ghost cell beyond the boundary with parameters ϱ, u, T equal to the $\varrho(1), -u(1), T(1)$ where $(\varrho(1), u(1), T(1))$ are the parameters in the first cell. At the right boundary ($x = 20$), we also add a ghost cell where, at

each time step, we impose the macroscopic variables equal to $\varrho(t = 0)$, $u(t = 0)$, $T(t = 0)$ and the distribution function equal to a Maxwellian corresponding to these parameters for the kinetic scheme. The computation is stopped at the final time $t = 0.04$ s. There are 1000 cells in physical space and 140 cells in velocity space. Artificial boundaries in velocity space are put at velocities equal to -3600 m/s and 3600 m/s. The cut-off function h is initialized as $h = 1$ for x ranging from -20 to $-17.5 = a_1$ (kinetic region), $h = \frac{x - b_1}{a_1 - b_1}$ with $b_1 = -16$ (buffer zone) and $h = 0$ for $x > -16$ (fluid region).

The initial conditions are such that mass density $\varrho = 5 \times 10^{-7}$ kg/m^3, mean velocity $u = -900$ m/s and temperature $T = 273$ K. The Knudsen number ε at initialization is equal to $\varepsilon \simeq 5.5 \times 10^{-3}$. Since ε is not too small, this suggests us that a kinetic scheme is necessary in some zones of the domain. When the simulation begins, a shock starts to form and a non-equilibrium zone arises. We plot the solution after few time steps $t = 2 \times 10^{-3}$ s for the density (figure 2, top) and velocity (figure 3, top) to show that the parameters β and β_M are less than 1 near the boundary (figure 4, top left). Then, the shock starts to move towards the right and after few time steps, β and β_M near the left boundary tend to return to their original value 1. Sufficiently far away from the discontinuity, the fluid approximation becomes valid. Thus, the algorithm automatically introduces a second buffer zone $[a_2, b_2]$ (figures 2–5, middle). On the left-hand side of point a_2, $h = 1$ which means that the fluid equations alone are solved. All regions move according to the value of β computed in the kinetic zone. When β approaches the value 1 then h starts to diminish. We finally plot the results at $t = 0.04$ s at the end of the simulation, for the density (figure 2, bottom), mean velocity (figure 3, bottom), β and β_M (figure 4, bottom left), Knudsen number (figure 4, bottom right) and smoothness indicators (figure 5, bottom).

We repeat the simulation increasing the initial density to the value $\varrho = 10^{-5}$ kg/m^3. This yields a different initial Knudsen number $\varepsilon \simeq 2.7 \times 10^{-4}$ and gives different results. Now β and more importantly β_M remain close to 1 also in the vicinity of the shock. This means that the fluid equations must produce very similar results as the kinetic equations. After a few time steps, when the shock is formed and starts to move, $\beta \simeq 1$ and $\beta_M \simeq 1$ (figure 6, middle left). Then, the scheme automatically sets $h = 0$ and computes the solution entirely with the macroscopic model. We display the density, velocity, Knudsen number, equilibrium fractions β and β_M, smoothness indicators ψ and ϕ when $t = 2 \times 10^{-3}$ s on figure 6, and when $t = 0.02$ s on figure 7. The final solution ($t = 0.04$) is very close to the solution we can compute with a hydrodynamic scheme. So we do not display it.

We note that as reported in section 5.1 the parameter β gives sometimes results that could suggest a strong departure to equilibrium while β_M does not. The parameter β_M seems more accurate in describing the error between a fluid and a kinetic model.

6.3   Sod shock tube problem

We consider the classical Sod test with the same number of mesh points in physical and velocity spaces as in the previous test (1000 points in physical space and 140 points in velocity space). We only change the position of the artificial boundaries in velocity space and set it now to the values -2000 m/s and 2000 m/s. The initial value are such that mass density $\varrho_L = 5 \times 10^{-6}$ kg/m^3, mean velocity $u_L = 0$ m/s and temperature $T_L = 273.15$

K if $-20 \leq x \leq 0$, while $\varrho_R = 5 \times 0.125 \times 10^{-6}$ kg/m^3, $u_R = 0$ m/s, $T_R = 218.4$ K if $0 \leq x \leq 20$. The initial data for the kinetic model are taken in thermodynamical equilibrium. The Knudsen numbers at the beginning of the simulation are $\varepsilon_L \simeq 0.6 \times 10^{-3}$ and $\varepsilon_R \simeq 4.5 \times 10^{-3}$ to the left and right hand sides of the discontinuity respectively. We begin by defining a kinetic zone between the initial discontinuity ($h = 1$) and two buffer zones to the right $[a_1, b_1]$ and to the left $[a_2, b_2]$ of it. In the rest of the domain the solution is computed with the macroscopic model that corresponds to $h = 0$. We plot the results in terms of the density (figure 8) and mean velocity (figure 9). We also display the Knudsen number (figure 10 right) and the two equilibrium fractions β and β_M (figure 10 left). The smoothness indicators for the density and velocity are shown on figure 11. For each variable we plot the solution at three different times: $t = 0.002$ s (top), $t = 0.015$ s (middle) and at $t = 0.03$ s (bottom). During the computation, we notice that the region where $\beta < 1$ (figure 10 left, top and middle) grows. The algorithm makes the two buffer zones move accordingly in order to keep this zone inside the kinetic area. The gas is too rarefied and the rarefaction waves as well as the two other waves require the microscopic model (figure 8 and 9, bottom).

We repeat the simulation with different initial densities: $\varrho_L = 2 \times 10^{-5}$ kg/m^3 and $\varrho_R = 0.25 \times 10^{-5}$ kg/m^3. The two Knudsen numbers are $\varepsilon_L \simeq 0.18 \times 10^{-3}$ and $\varepsilon_R \simeq 1.1 \times 10^{-3}$. This leads to different final results. The initial cut-off function h is chosen as previously, but now the Knudsen numbers are such that the distribution function relaxes more rapidly towards equilibrium and the macroscopic model is sufficiently accurate except in the vicinity of the contact discontinuity and shock wave. Again, we display the density (figure 12), mean velocity (figure 13), Knudsen number (figure 14 right), equilibrium fractions (figure 14 left) and smoothness indicators (figure 15) at the same instants as in the previous simulation. At the beginning of the simulation, the rarefaction wave lies within the kinetic region (see figures 12-13 top, middle). As time evolves, the rarefaction wave leaves the kinetic region to end in the fluid region (figures 12-13 bottom). The error between the macroscopic and the microscopic models in this region is very small.

¿From our tests, we can conclude that the equilibrium parameter β_M seems to be a more precise indicator of local equilibrium than β. Using β_M to characterize equilibrium regions seems a promising strategy for the future developments of the coupling method and application to numerical simulations of transition regimes from rarefied to dense flows.

6.4   Use of a different scheme for the fluid-dynamical part

In this section we show how the coupling model behaves when used in conjunction with a different scheme for the fluid-dynamical part. We repeat the computations of the two previous sections, namely the unsteady shock test problem and the Sod shock tube problem. For the unsteady shock test problem, the initial values are $\varrho = 5 \times 10^{-6}$ kg/m^3, mean velocity $u = -900$ m/s and temperature $T = 273$ K, while for the Sod shock test problem, they are $\varrho_L = 2 \times 10^{-5}$ kg/m^3, $u_L = 0$ m/s, $T_L = 273.15$ K and $\varrho_R = 0.25 \times 10^{-5}$ kg/m^3, $u_L = 0$ m/s, $T_L = 273.15$ K. We use the same meshes in physical and velocity spaces as previously. We only plot the results for the density and velocity at different time steps. Figure 16 for the Sod shock tube problem and figure 17 for the unsteady shock problem

show that the solution agrees well with the previous results except for small differences due to the different numerical scheme. The computational time of the two simulations on a 3 Ghz Athlon computer shows a speedup of 65 % for the Sod problem and of 40 % for the unsteady shock problem. This different speedup can be explained by the different sizes of the kinetic regions in the two tests, and also by the different time steps. In the second test, the limitation of the time step due to convection (CFL condition) and that coming from the relaxation are close. Therefore, the simulation times for the macroscopic and microscopic models are closer than in the case of the Sod test. These considerations suggest that the use of such a decomposition technique is very efficient in regimes close to thermodynamical equilibrium in which however, Navier-Stokes or Euler fail to accurately describe the flow. Such regimes are the so-called transitional regimes. Of course, the computational time can be reduced even further for two or three dimensional computations.

7   Conclusion

In this work we have proposed a new approach for the solution of rarefied gas dynamics problems through a dynamic coupling of kinetic and fluid equations. This method extends previous works [6] where a static coupling was considered. The main feature of the work is that the two models are coupled in a region in which the full solution is recovered by summing up the two (kinetic and fluid) contributions. One advantage of this technique is that no boundary condition is needed at the boundary of each zone, by contrast to conventional domain decomposition schemes. This makes the method very flexible. In the present work, we have proposed a procedure to dynamically update the location of the different fluid and kinetic regions. This allows a time adaptation of the domain decomposition technique which dramatically increases the efficiency of the method. Another important feature of the method which has been highlighted in the present work is the possibility of creating new kinetic regions (in other words, the topology of the domain decomposition itself can be dynamically updated). The combination of different criteria both of macroscopic and microscopic nature allows to reliably detect the regions of sharp gradients and discontinuities where the microscopic model must be solved and we can define a priori the approximation tolerance that we decide to accept.

The last part of the paper is devoted to numerical tests in order to compare the performances and results of the coupling method with respect to both the macroscopic and microscopic models. Although only one-dimensional results have been presented, and further tests must be performed to completely validate the method, the results look very encouraging. The algorithm performs well with the two different numerical schemes that have been experimented and significant computational speedup can be achieved without compromising the accuracy of the results. Compared to a steady domain decomposition method, the possibility of dynamically updating the kinetic region allows us to shrink the kinetic zones to the region of interest at any time which results in considerably improved efficiency.

In the future, the numerical tests need to be extended to two dimensional problems.

The dynamic domain decomposition strategy will also be adapted to different coupling methods such the localized kinetic upscaling method of Degond, Liu and Mieussens [8], or the hybrid domain decomposition method developed by Dimarco and Pareschi [10] where a Monte Carlo scheme is used to compute the solution of the Boltzmann-BGK equations.

References

[1] J. F. Bourgat, P. LeTallec, B. Perthame, and Y. Qiu, *Coupling Boltzmann and Euler equations without overlapping*, in Domain Decomposition Methods in Science and Engineering, Contemp. Math. 157, AMS, Providence, RI, (1994), pp. 377–398.

[2] R. E. Caflisch, *Monte Carlo and Quasi-Monte Carlo Methods*, Acta Numerica (1998) pp. 1–49.

[3] C. Cercignani, R. Illner, M. Pulvirenti, The mathematical theory of dilute gases. Springer-Verlag, New York, (1995).

[4] G. Q. Chen, D. Levermore and T. P. Liu, *Hyperbolic conservation laws with stiff relaxation terms and entropy*, Comm. Pure Appl. Math., 47 (1994), pp. 787–830.

[5] N.Crouseilles, P.Degond, M.Lemou, *A hybrid kinetic-fluid model for solving the gas-dynamics Boltzmann BGK equation*, Journal of Computational Physics 199 (2004) 776-808.

[6] P.Degond, S.Jin, L. Mieussens, *A Smooth Transition Between Kinetic and Hydrodynamic Equations* , Journal of Computational Physics 209 (2005) 665–694.

[7] P.Degond and S.Jin, *A Smooth Transition Between Kinetic and Diffusion Equations*, SIAM journal on numerical analysis 2005, vol. 42, no6, pp. 2671-2687 .

[8] P.Degond, J.G. Liu, L. Mieussens, *Macroscopic Fluid Model with Localized Kinetic Upscaling Effects*, MMS 5(3), 940–979 (2006)

[9] G. Dimarco and L. Pareschi, *Hybrid multiscale methods II. Kinetic Equations*, Submitted to SIAM J. of Multiscale Modeling and Simulation.

[10] G. Dimarco and L. Pareschi, *Domain Decomposition Techniques and Hybrid Multiscale Methods for kinetic equations*, Hyperbolic 2006 Proceeding, to appear.

[11] W. E and B. Engquist, *The heterogeneous multiscale methods*, Comm. Math. Sci., 1, (2003), pp. 87-133.

[12] W. E and B. Engquist, *The heterogeneous multiscale method for homogenization problems*, Lecture Notes in Computational Science and Engineering, Vol.44, pp. 89–110, (2006).

[13] W. E and B. Engquist, *Multiscale Modeling and Computation*, Notices of the AMS, 50(9), (2003), pp. 1062–1070.

[14] A. B. Huang and P. F. Hwang, *Test of statistical models for gases with and without internal energy states*, Physics of Fluids, 16(4):466475, 1973.

[15] V.I. Kolobov, R.R. Arslanbekov,V.V. Aristov, A.A. Frolova, S.A. Zabelok, *Unified Solver for Rarefied and Continuum Flows with Adaptive Mesh and Algorithm Refinement*, Journal of Computational Physics Vol. 223 No. 2, pp. 589–608 (2007).

[16] M.A. KATSOULAKIS, A.J. MAJDA AND A. SOPASAKIS, *Multiscale Couplings In Prototype Hybrid Deterministic/Stochastic Systems: Part I, Deterministic Closures*, Comm. Math. Sci., Vol. 2, No. 2, (2004), pp. 255-294.

[17] D. LEVERMORE, W.J.MOROKOFF, B.T. NADIGA, *Moment realizability and the validity of the NavierStokes equations for rarefied gas dynamics*, Physics of Fluids, Vol. 10, No. 12, (1998).

[18] L. MIEUSSENS, *Discrete Velocity Model and Implicit Scheme for the BGK Equation of Rarefied Gas Dynamic* ,Mathematical Models and Methods in Applied Sciences, Vol 10 No. 8 (2000) 1121-1149.

[19] L. MIEUSSENS, *Discrete Velocity Model and numerical schemes for the Boltzmann-BGK equation in plane and axisymmetric geometries*, J. Comput. Phys., Vol. 162, 429-466, 2000.

[20] L. MIEUSSENS, Convergence of a discrete-velocity model for the Boltzmann-BGK equation. *Comput. Math. Appl.*, 41(1-2):83–96, 2001.

[21] P. LETALLEC AND F. MALLINGER, *Coupling Boltzmann and Navier-Stokes by half fluxes* Journal of Computational Physics, 136, (1997) pp. 51–67.

[22] R. J. LEVEQUE, *Numerical Methods for Conservation Laws*, Lectures in Mathematics, Birkhauser Verlag, Basel (1992).

[23] R. NATALINI, *Convergence to equilibrium for relaxation approximations of conservation laws.* Comm. Pure Appl. Math. **49** (1996) pp. 795–823.

[24] L. PARESCHI AND R. E. CAFLISCH, *Implicit Monte Carlo methods for rarefied gas dynamics I: The space homogeneous case*, J. Comput. Phys., 154 (1999), pp. 90–116.

[25] L. PARESCHI AND R. E. CAFLISCH, *Towards a hybrid method for rarefied gas dynamics*, IMA Vol. App. Math. 135, (2004), pp. 57–73.

[26] L. PARESCHI, *Hybrid multiscale methods for hyperbolic and kinetic problems*, Esaim Proceedings Vol. 15, EDP Sciences, SMAI (2005) pp. 87–120.

[27] B. PERTHAME, *Boltzmann type schemes for gas dynamics and the entropy property*, SIAM J. Num. Anal., vol. 27, (1990), pp.1405-1421.

[28] S. TIWARI, *Coupling of the Boltzmann and Euler equations with automatic domain decomposition*, J. Comput. Phys., vol. 144, 1998, 710–726.

[29] W.-L. WANG AND I. D. BOYD, *Predicting Continuum breakdown in Hypersonic Viscous Flows*, Physics of Fluids, Vol. 15, 2003, pp 91-100.
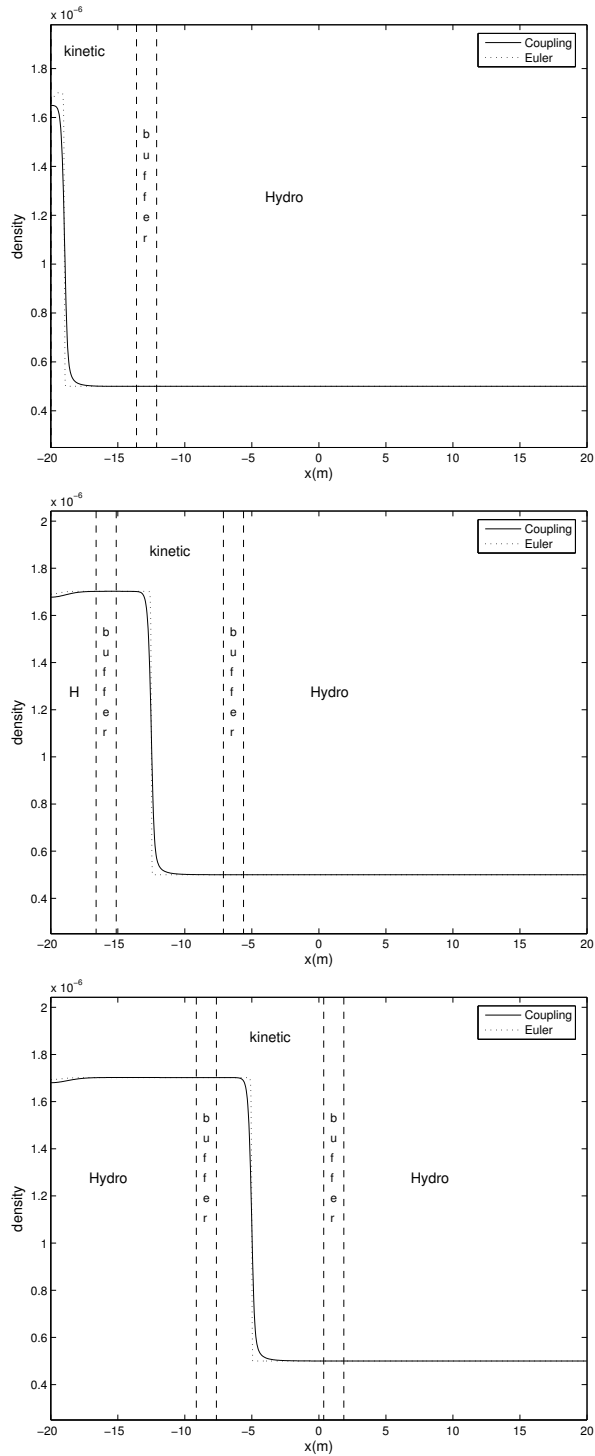
Figure 2: Unsteady Shock 1: Density profile at different times $t = 0.002$ (top), $t = 0.02$ (middle), $t = 0.04$ (bottom). The solid line is the solution of the coupling model, the dotted line is that of the Euler system.
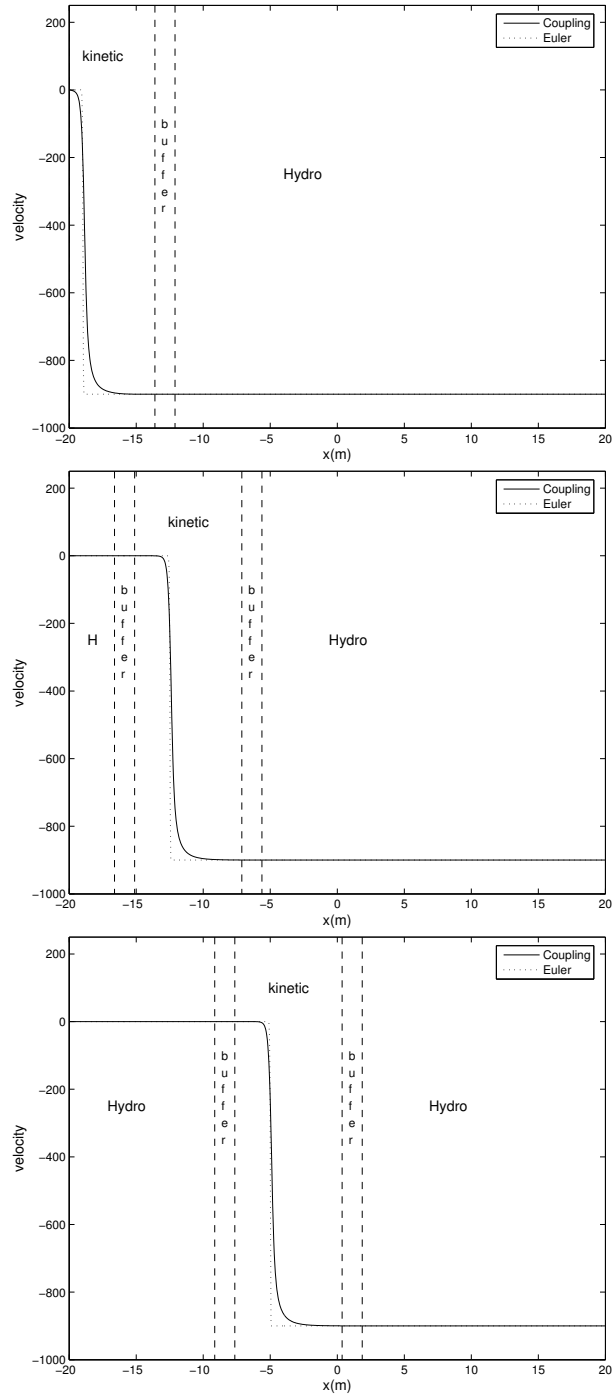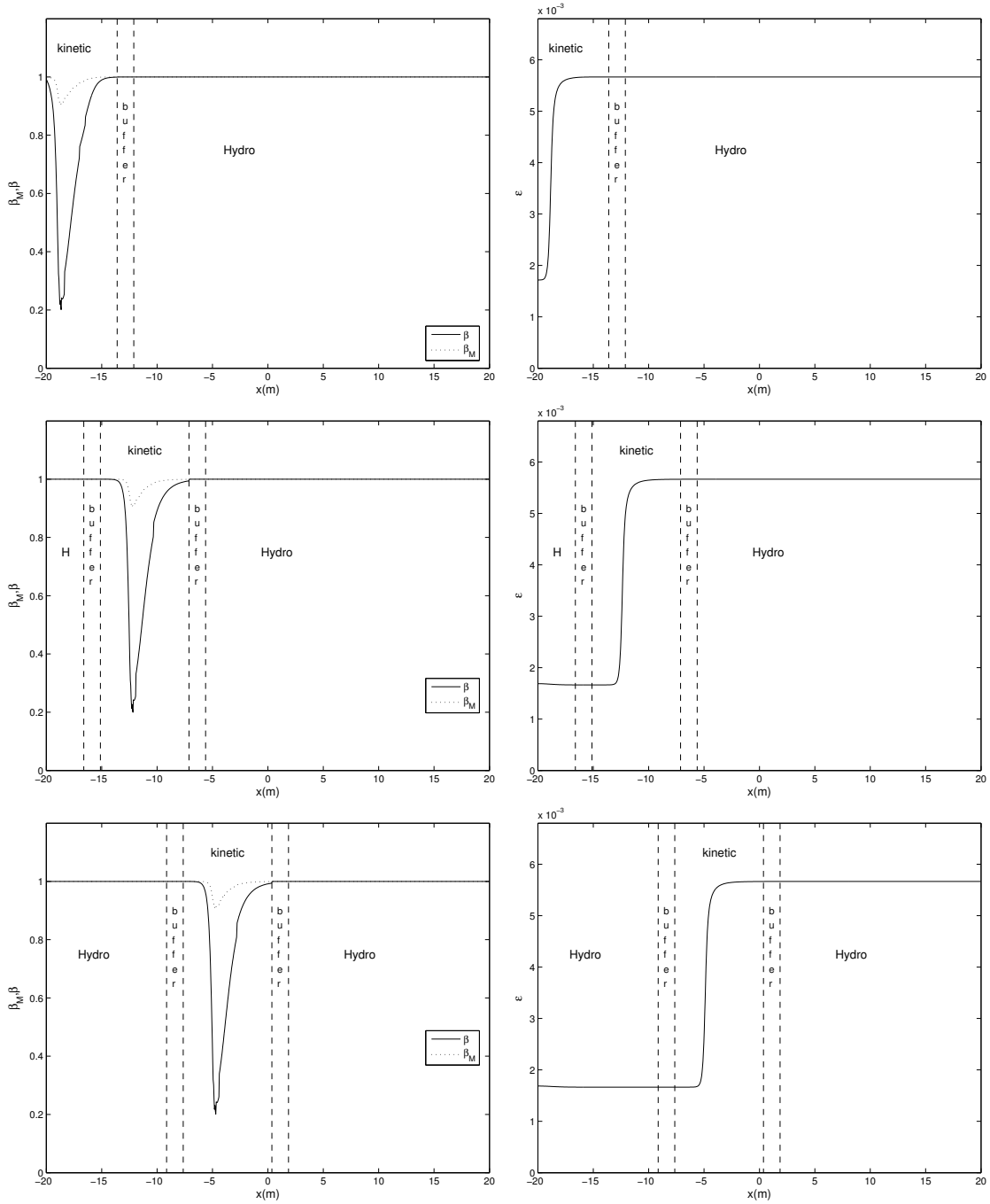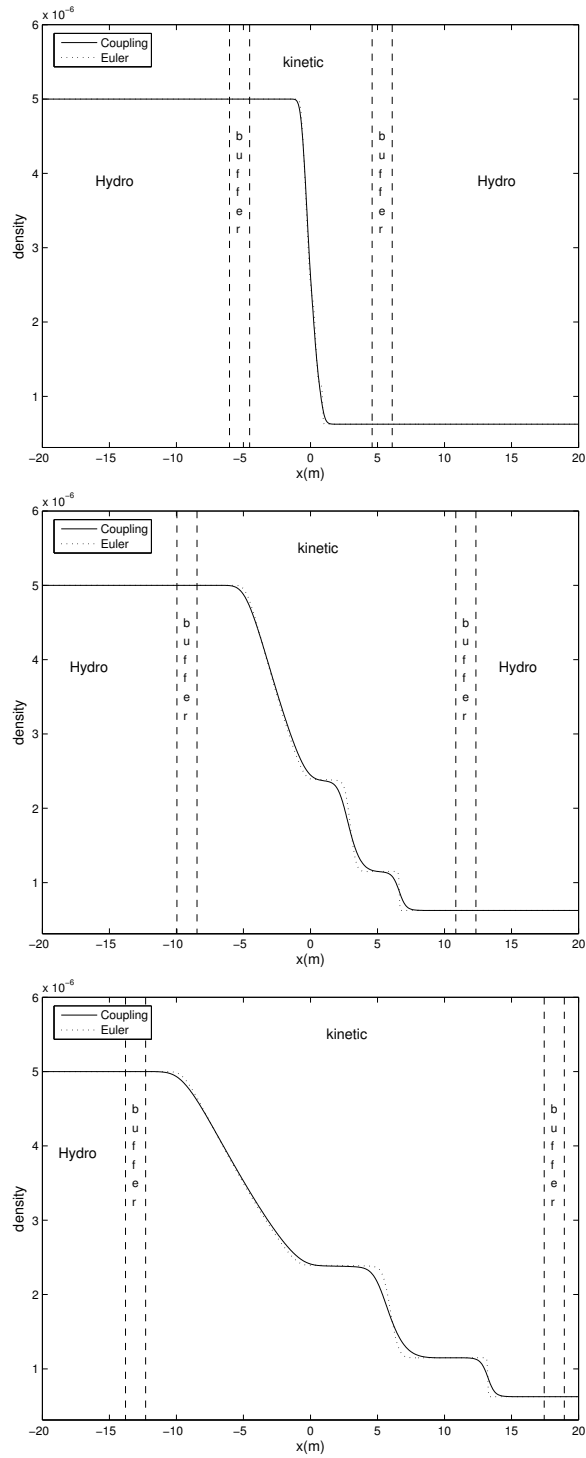
Figure 3: Unsteady Shock 1: Velocity profile at different times $t = 0.002$ (top), $t = 0.02$ (middle), $t = 0.04$ (bottom). The solid line is the solution of the coupling model, the dotted line is that of the Euler system.
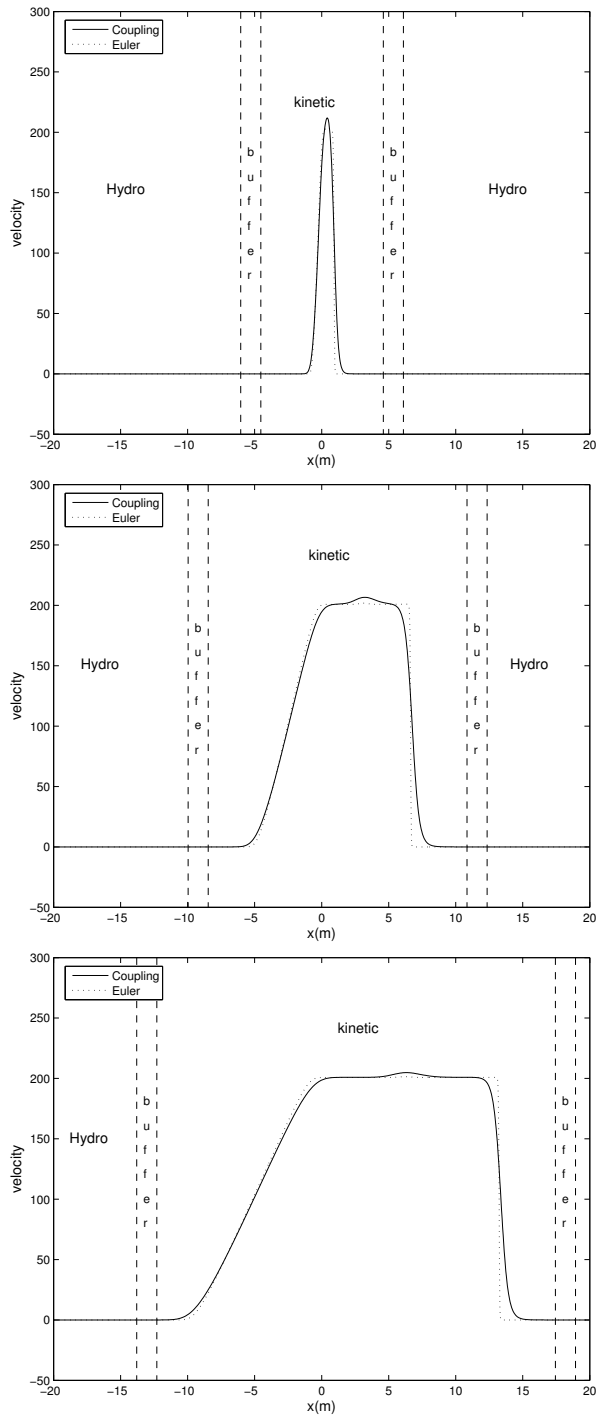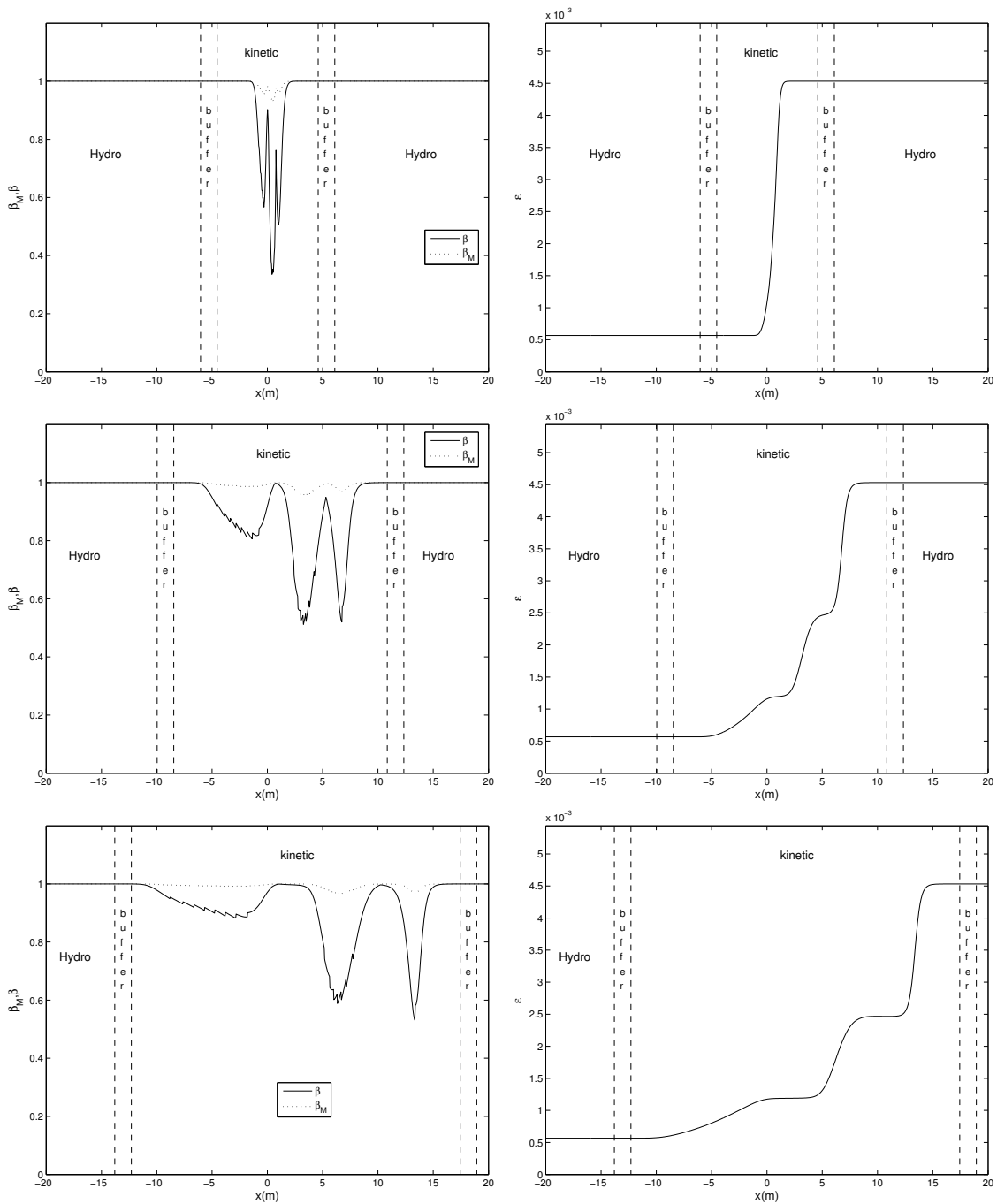
26

Figure 4: Unsteady Shock 1: Equilibrium fraction profile (left), Knudsen number (right) at different times $t = 0.002$ (top), $t = 0.02$ (middle), $t = 0.04$ (bottom).
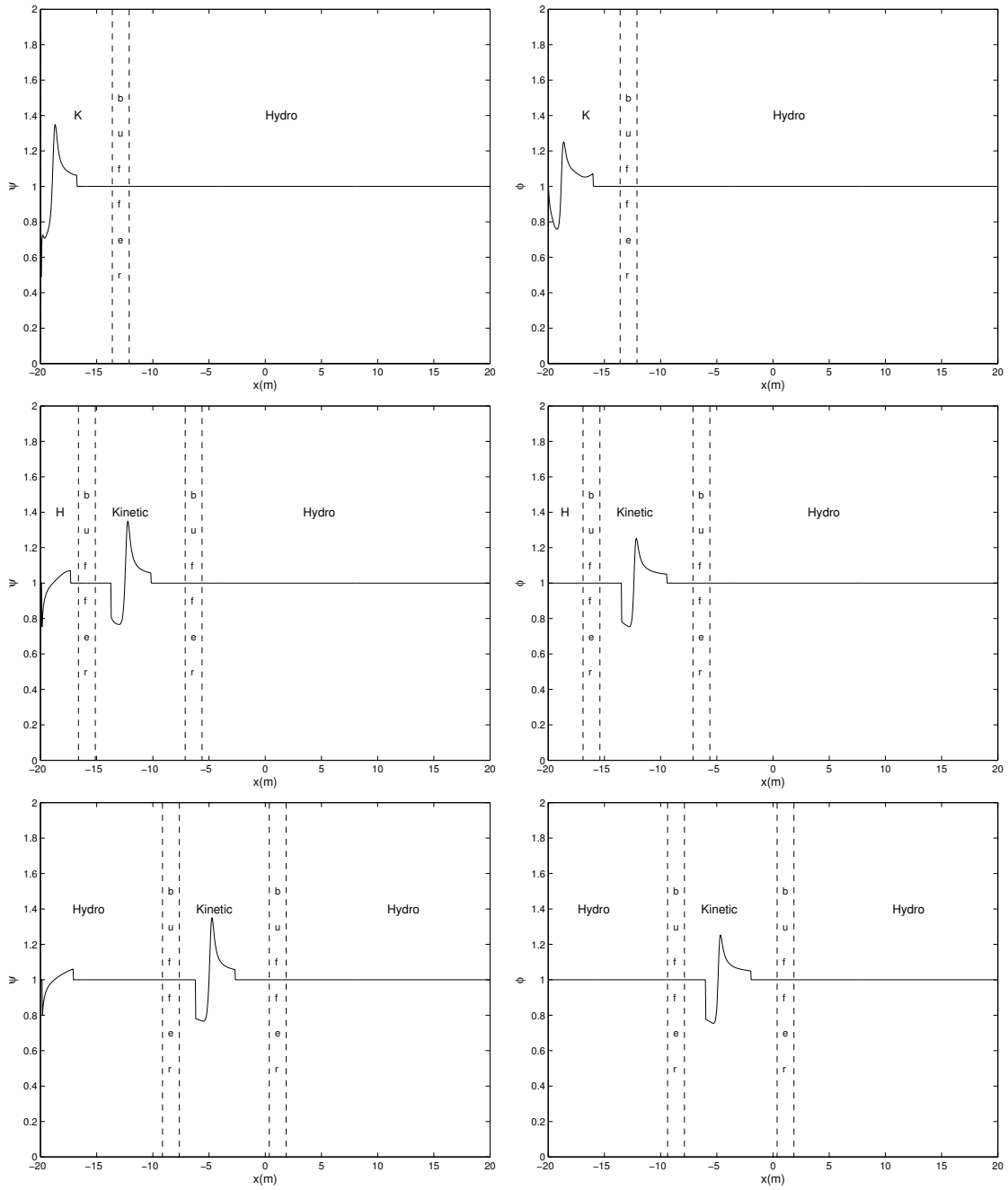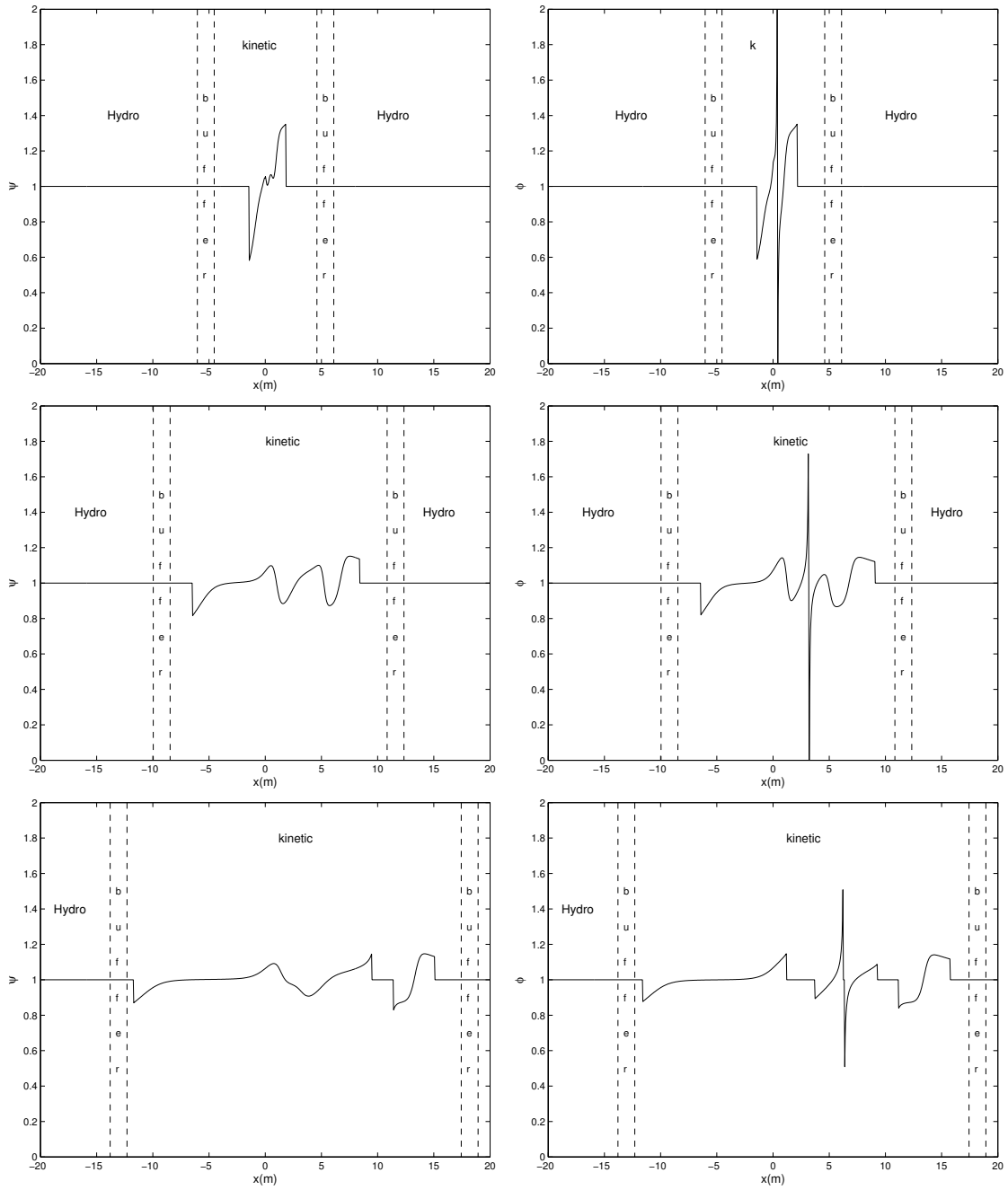
Figure 5: Unsteady Shock 1: Smoothness indicators for density (left) and velocity (right) at different times $t = 0.002$ (top), $t = 0.02$ (middle), $t = 0.04$ (bottom)

28
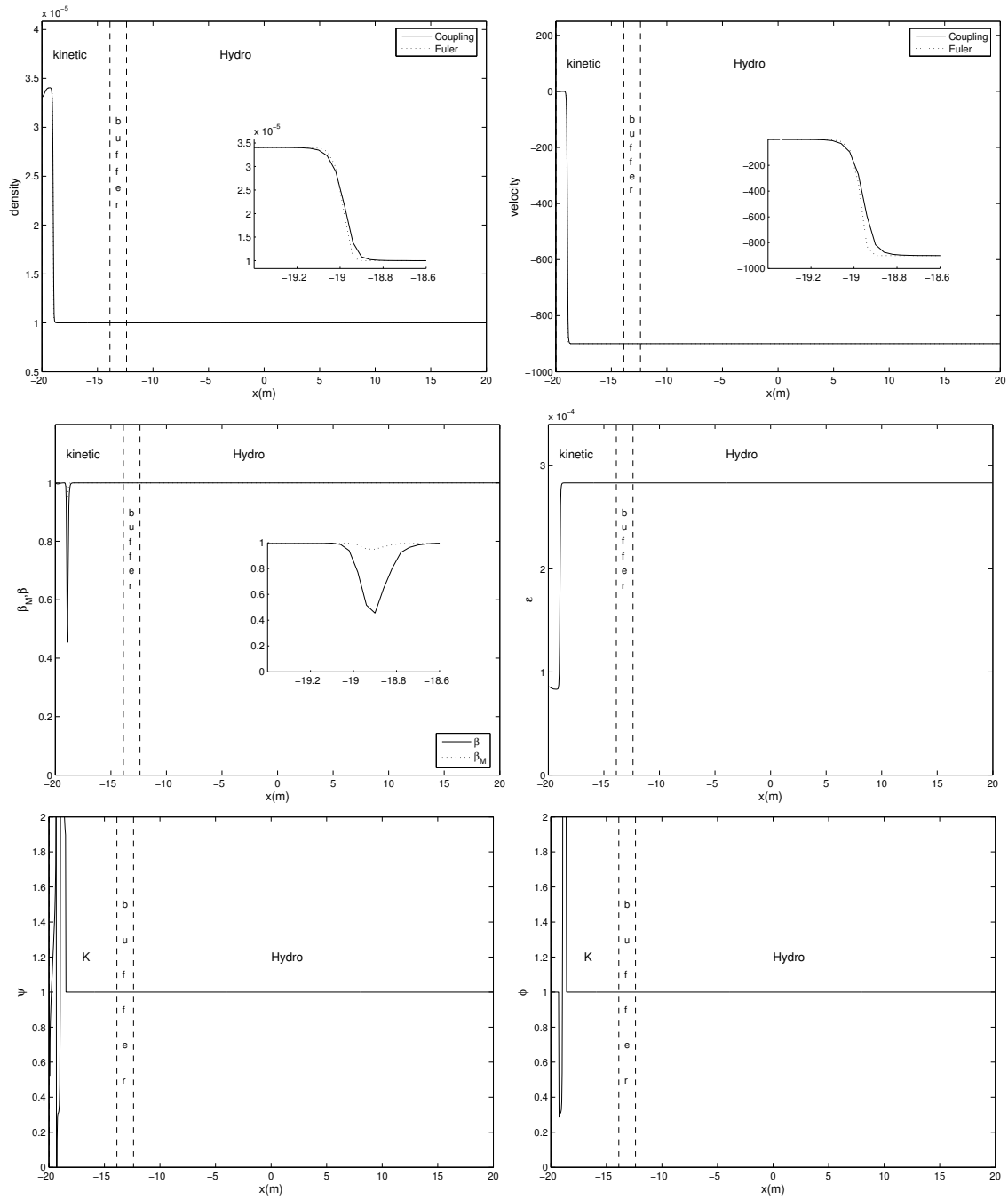
Figure 6: Unsteady Shock 2: Solution at $t = 2 \times 10^{-3}$. Density (top left), velocity (top right), equilibrium fraction (middle left), Knudsen number (middle right), density smoothness indicator (bottom left), velocity smoothness indicator (bottom right). The small panels are a magnification of the solution close to the shock.
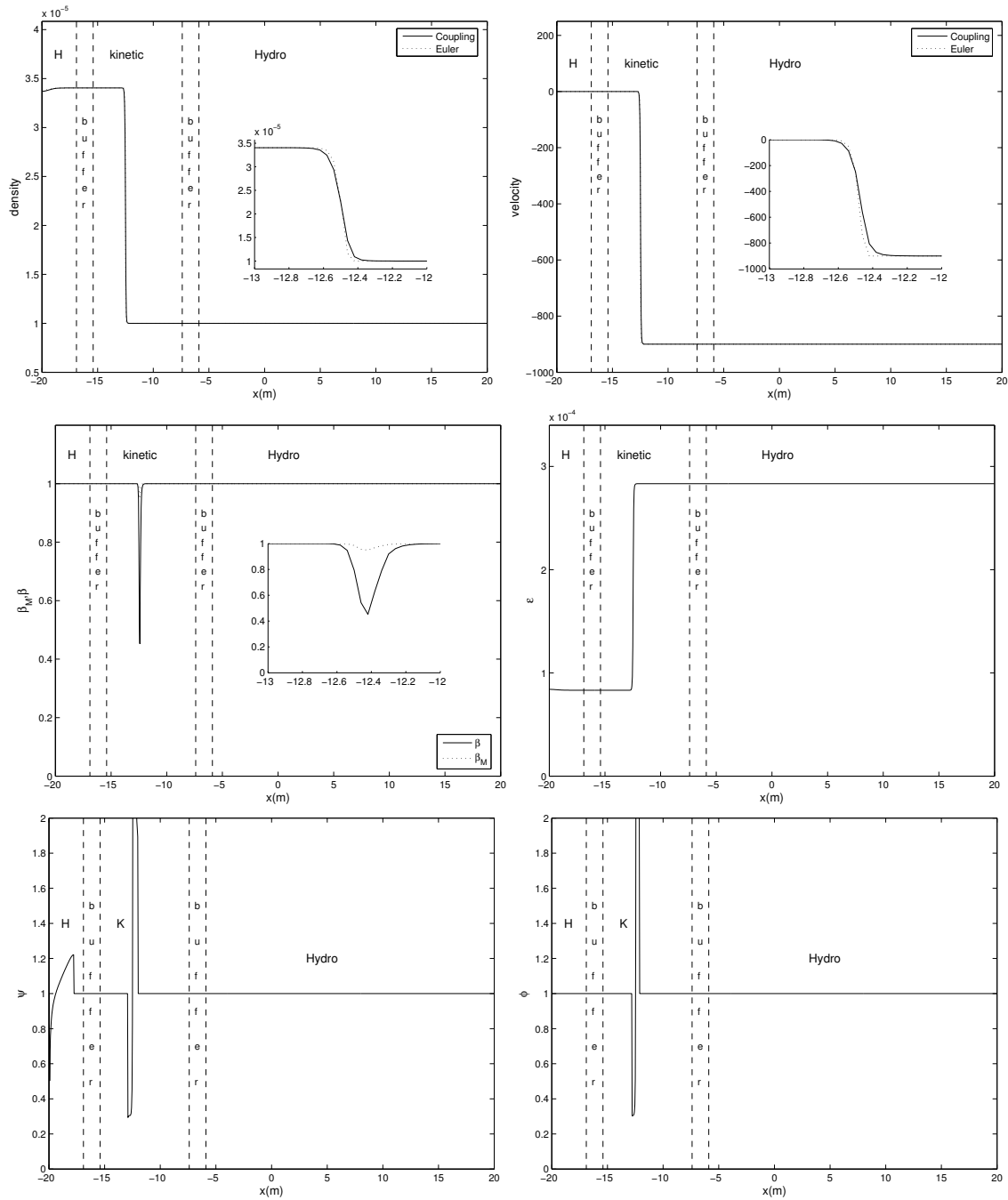
Figure 7: Unsteady Shock 2: Solution at $t = 0.02$. Density (top left), velocity (top right), equilibrium fraction (middle left), Knudsen number (middle right), density smoothness indicator (bottom left), velocity smoothness indicator (bottom right). The small panels are a magnification of the solution close to the shock.
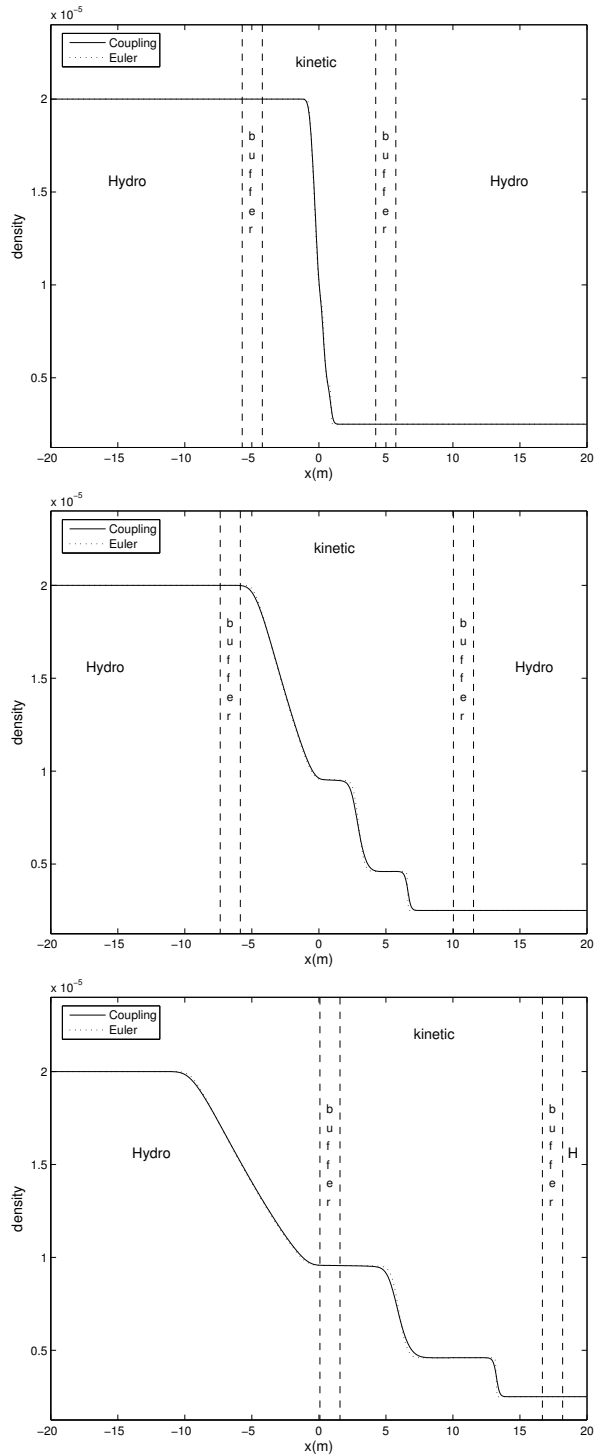
30

Figure 8: Sod test 1: Density profile at different times $t = 0.002$ (top), $t = 0.015$ (middle), $t = 0.03$ (bottom). The solid line is the solution of the coupling model, the dotted line is that of the Euler system.

31

Figure 9: Sod test 1: Velocity profile at different times $t = 0.002$ (top), $t = 0.015$ (middle), $t = 0.03$ (bottom). The solid line is the solution of the coupling model, the dotted line is that of the Euler system.
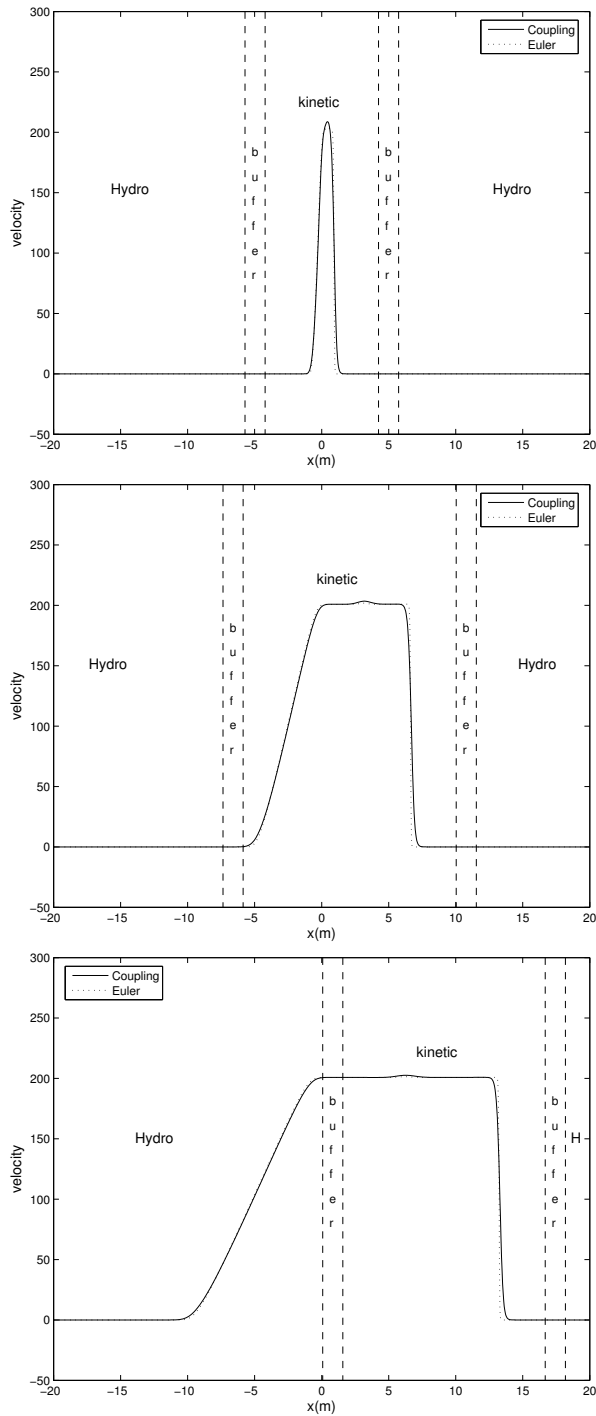
Figure 10: Sod test 1: Equilibrium fraction profile (left), Knudsen number (right) at different times $t = 0.002$ (top), $t = 0.015$ (middle), $t = 0.03$ (bottom).

Figure 11: Sod test 1: Smoothness indicators for density (left) and velocity (right) at different times $t = 0.002$ (top), $t = 0.015$ (middle), $t = 0.03$ (bottom)

Figure 12: Sod test 2: Density profile at different times $t = 0.002$ (top), $t = 0.015$ (middle), $t = 0.03$ (bottom). The solid line is the solution of the coupling model, the dotted line is that of the Euler system.
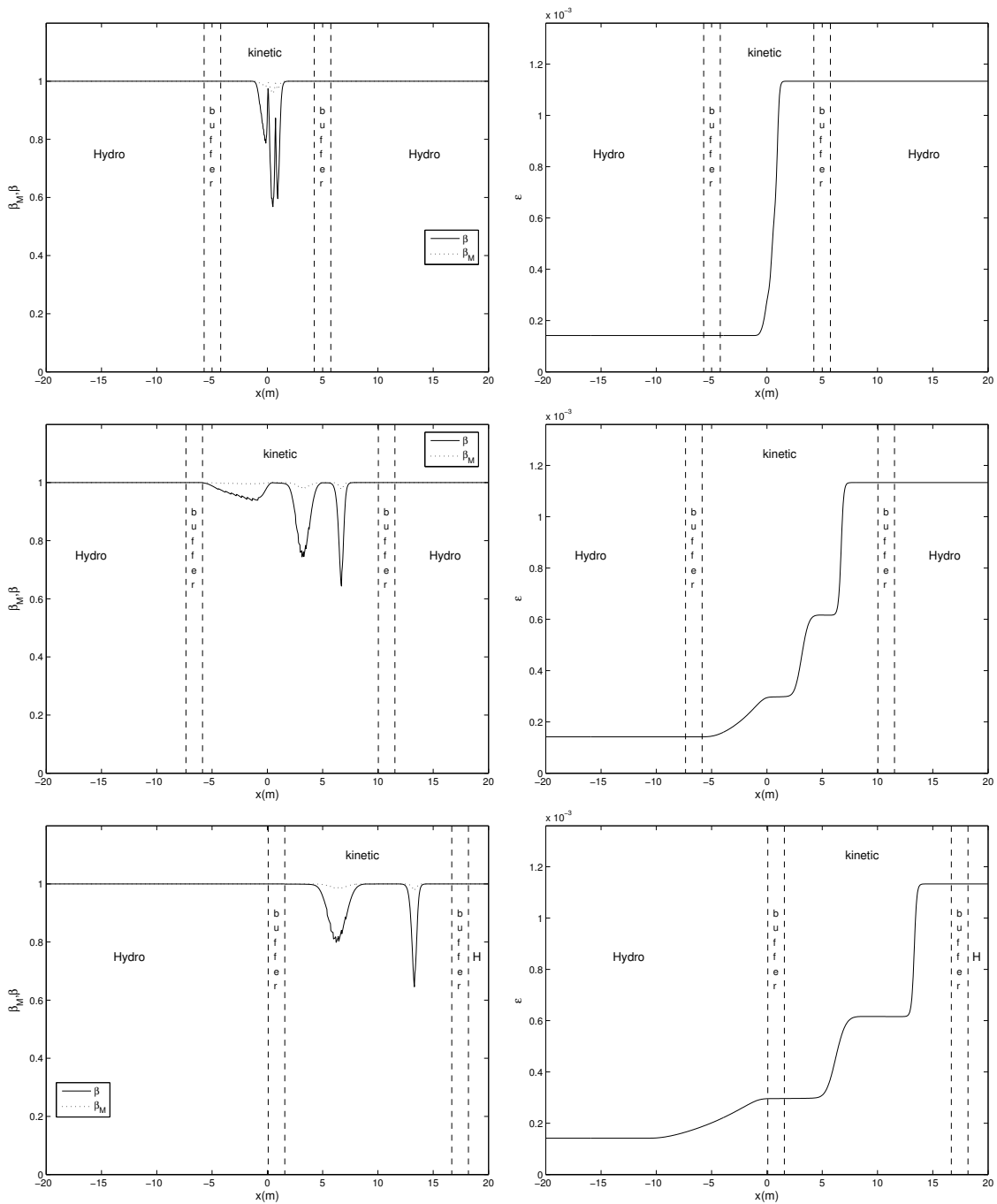
Figure 13: Sod test 2: Velocity profile at different times $t = 0.002$ (top), $t = 0.015$ (middle), $t = 0.03$ (bottom). The solid line is the solution of the coupling model, the dotted line is that of the Euler system.

36

Figure 14: Sod test 2: Equilibrium fraction profile (left), Knudsen number (right) at different times $t = 0.002$ (top), $t = 0.015$ (middle), $t = 0.03$ (bottom).
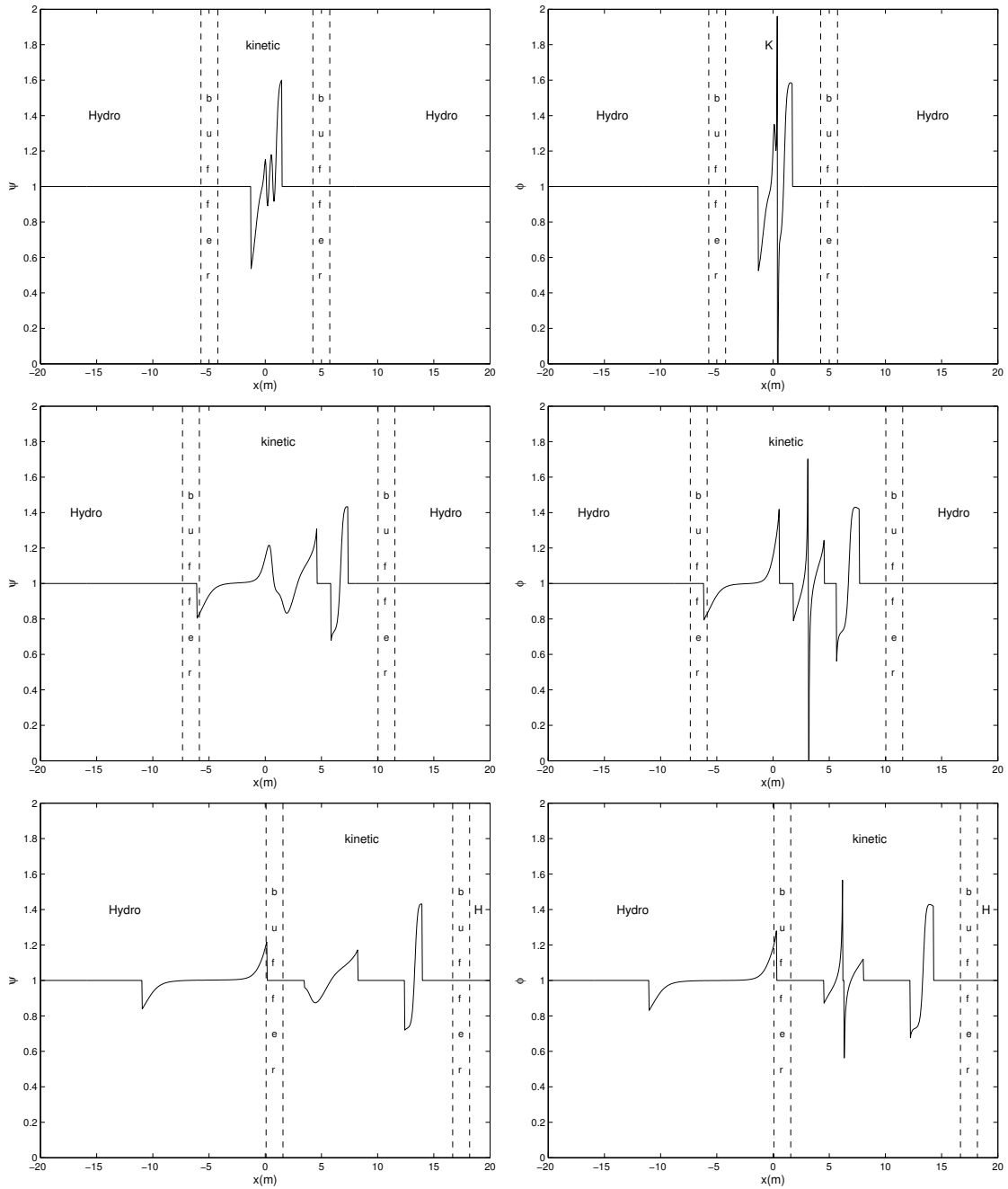
Figure 15: Sod test 2: Smoothness indicators for density (left) and velocity (right) at different times $t = 0.002$ (top), $t = 0.015$ (middle), $t = 0.03$ (bottom)
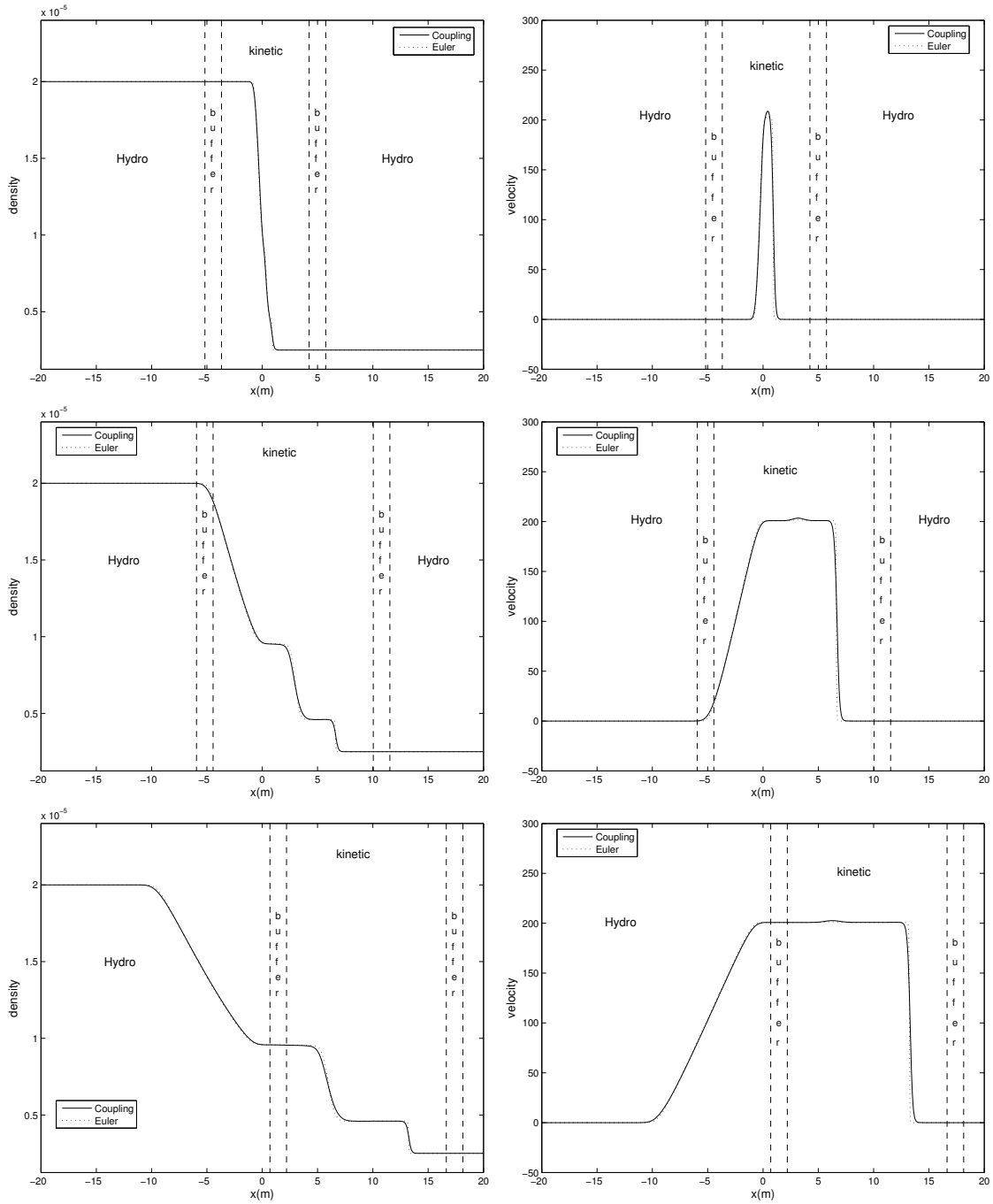
Figure 16: Sod Test 3: Density (left), Velocity (right) profiles at different times $t = 0.002$ (top), $t = 0.015$ (middle), $t = 0.03$ (bottom). The solid line is the solution of the coupling model, the dotted line is that of the Euler system.
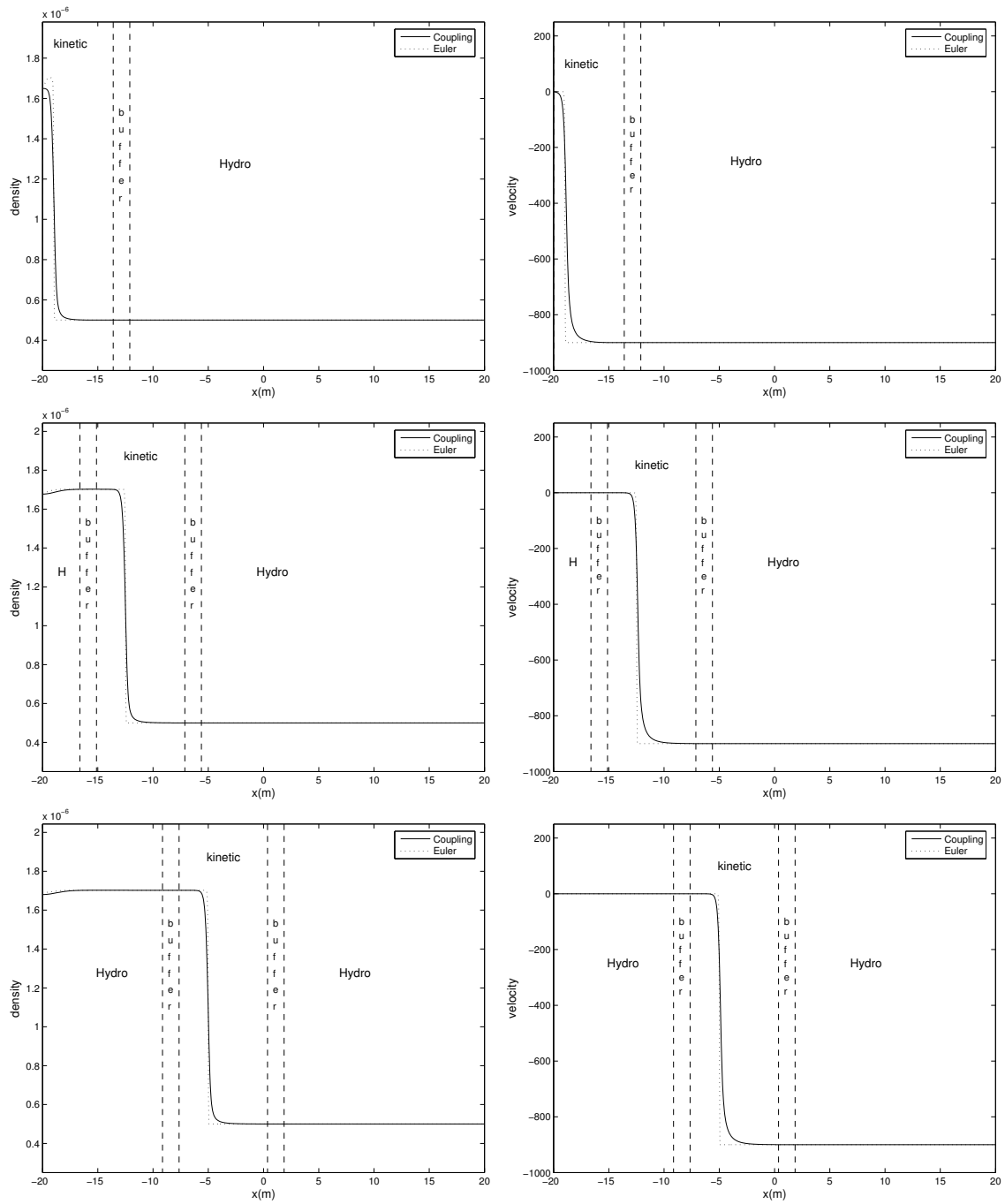
Figure 17: Unsteady shock test: Density (left), Velocity (right) profiles at different times $t = 0.002$ (top), $t = 0.02$ (middle), $t = 0.04$ (bottom). The solid line is the solution of the coupling model, the dotted line is that of the Euler system.